UNIVERSITY OF CALIFORNIA, SAN DIEGO

Modeling and Experimentation of a Ribbed Caudal Fin With Applications in Aquatic Robots

A Thesis submitted in partial satisfaction of the
requirements for the degree of Master of Science

in

Engineering Sciences (Mechanical Engineering)

by

Ardavan Amini

Committee in charge:

Professor Hidenori Murakami, Chair
Professor Nicholas G. Gravish
Professor James D. Hollan

2017

The thesis of Ardavan Amini is approved, and is acceptable in quality and form for publication on microfilm and electronically:

_____

_____

_____

Chair

University of California, San Diego

2017

TABLE OF CONTENTS

LIST OF FIGURES

ACKNOWLEDGEMENTS

I would like to thank my advisor, Professor Hidenori Murakami, for the opportunities he has given me over the years and trusting in my abilities at every turn.

I would also like to thank Mr. Oscar Rios for being the greatest lab mate anyone could ask for. His support and encouragement has helped me immensely.

Lastly, I would like to thank my mother, Ms. Fariba Fasihi, for always being there for me, believing in me, and giving me the confidence to achieve my goals in life; love you mom!

Chapter 2, in part, has been submitted for publication of the material as it may appear in the International Mechanical Engineering Congress and Exposition 2017. Rios, Oscar; Amini, Ardavan; Murakami, Hidenori.

ABSTRACT OF THE THESIS

Modeling and Experimentation of a Ribbed Caudal Fin With Applications in Aquatic Robots

by

Ardavan Amini

Master of Science in Engineering Sciences (Mechanical Engineering)

University of California, San Diego, 2017

Professor Hidenori Murakami, Chair

Presented in this study is a mathematical model and preliminary experimental results of a ribbed caudal fin to be used in an aquatic robot. The ribbed caudal tail is comprised of two thin beams separated by ribbed sectionals as it tapers towards the fin. By

oscillating the ribbed caudal fin, the aquatic robot can achieve forward propulsion and maneuver around its environment. The fully enclosed system allows for the aquatic robot to have very little effect on marine life and fully blend into its respective environment. Because of these advantages, there are many applications including surveillance, sensing, and detection.

Because the caudal fin actuator has very thin side walls, Kirchhoff-Love's large deformation beam theory is applicable for the large deformation of the fish-fin actuator. In the model, it is critical to accurately model the curvature of beams. To this end, C^1 beam elements for thin beams are developed by specializing the shear-deformable beam elements, [19], based upon Reissner's shear-deformable nonlinear beam model. Furthermore, preliminary experiments on the ribbed fin are presented to supplement the FE model.

Uses for underwater robots are widespread, impacting many engineering and commercial sectors. To achieve maximum maneuverability, several means of propulsion have been discussed and implemented in existing robots. Presented in this research is an alternative method of generating propulsion through the use of gyroscopes. Gyroscopes have been widely known as a means of stabilization or attitude control. In the work presented, a gyroscopically driven robot design is shown and validated through experiments. The robot was shown to swim along a straight path and perform both left and right 90 and 180 degree turns, allowing it to successfully maneuver along the water surface plane.

CHAPTER 1: INTRODUCTION

Uses for aquatic robots are widespread, impacting military, commercial, oceanographic, and engineering research. To achieve maximum maneuverability, several means of propulsion and fin designs have been discussed and implemented in existing technology. Previous works in aquatic biomimetic robots have been able to actuate the caudal and or the posterior of the robot enclosed in either a hard casing or soft membrane. The tails proposed all include jointed segments, where each joint is driven by a servo to achieve the oscillatory motion needed for forward propulsion [1-3]. While the proposed ideas provide the results needed, they don't exemplify the natural motion and movement of a fish. Other methods of actuation and tail designs have been proposed that are able to use pneumatics and hydraulics to actuate a soft single body [4,5]. Although these robotic fish driven by fluidic elastomer actuation or pressurized air can perform quick maneuvers and achieve motion that closely resembles that of a fish, the manufacturing of these soft bodied actuators can be time consuming. Proposed in this paper is a ribbed caudal fin that is comprised of two thin beams separated by a varying number of webs or ribbed sectionals to increase or decrease the stiffness. By actuating the first web through a servo, as done in the preliminary experiments presented below, or by any other mechanism design, a large oscillatory motion is created that produces the necessary forward thrust.

To properly model the caudal fin, the Kirchhoff-Love beam equations, which neglect the transverse shear deformation, will be used. To systematically show the derivation of the equations, the moving frame method will be first used to derive Reissner's shear deformable equations from which we will then simplify to obtain the Kirchhoff-Love

equations. To solve the nonlinear equations numerically, the principal of virtual work and the nonlinear finite element equations, through the use of C^1beam elements, are derived.

The development of autonomous underwater vehicles (AUVs) and aquatic biomimetic robotics, is of great importance for the field of engineering. Uses for underwater robots in general are widespread, impacting military, commercial, oceanographic, and engineering research. To achieve maximum maneuverability, several means of propulsion have been discussed and implemented in existing technology. Previous works in aquatic biomimetic robots have been able to use servos to actuate the caudal and or the posterior of the robot enclosed in either a hard casing or soft membrane [1-3]. Other previous work was able to use pneumatics and hydraulics to actuate the soft-bodied exterior [4,5]. Presented in this research is an alternative and novel method of generating propulsion through the use of gyroscopes.

Previous work has shown and proven gyroscopes as a means of stabilization and ocean wave energy harvesting [17-20]. Traditionally, gyroscopic stabilization is achieved by rotating the gimbal to create a reactionary torque on the outer body; however, gyroscopes may be used in a different manner. In this paper, rather than to orient, gyroscopes will be presented as a mean of generating propulsion and as a means of maneuvering.

There are several benefits of using gyroscopes as a means of propulsion. The systems is self-contained and completely enclosed, allowing for control of noise and visual appearance. The use of gyroscopes more importantly provides various parameters that can be controlled to optimize output torque and maneuverability. With a gyroscopic design, we avoid the use of linkages, providing little maintenance needs and moving

components. Also, the use of a gyroscopes allows for a more flexible design that can be continually improved upon with respect to the programming, fin design, and overall body design.

An important factor in the implementation of this underwater robot is working through the iterative design process. On this end, a prototype of a gyroscopically driven aquatic robot is developed and tested. Results were measured and observed that lead to continually improving multiple aspects of the device. This way, a more efficient underwater robot can be created, which is optimized with respect to the programming and overall design of the system. In these initial iterations, the device is remotely controlled while in the water. An XBee module is connected to an Arduino microcontroller, which allows commands to be sent to the robot without the need of tethering.

Initial water tank tests were conducted to demonstrate the capabilities of the gyroscopically driven robot. The robot was shown to successfully maneuver anywhere along the water surface. It was capable of performing precise turns and move in fairly straight path when moving forward. Tests were conducted with a small, semi-rigid fin and a flexible caudal fin. From the water tank tests, several improvements to the system can be considered for future designs: Better features to maintain the correct orientation of the robot for maximum propulsion, more efficient use of programming to ensure less power is lost, and deciding on the most effective fin design. With the results of the experiments conducted, a more complete robot can be designed and implemented, which can have broad applications from data acquisition to surveilling. Also, future iterations of the design will shift toward autonomous control rather than remotely controlled, as it is currently.

CHAPTER 2: CAUDAL FIN

2.1 Ribbed Caudal Fin

The ribbed caudal fin that will be analyzed consists of two thin beams separated by webs. The webs are assumed to be thin, rigid, and always perpendicular to the beams as the fin is actuated. Shown in Fig. 2.1 are three different views of the caudal fin that will be analyzed with zero, one, and two webs. The proximal web is driven to induce large elastic oscillations of the caudal-fin actuator to induce a thrust for an aquatic fish robot. In the sections to follow, the mathematical model of the ribbed caudal fin will be derived along with the finite element equations.

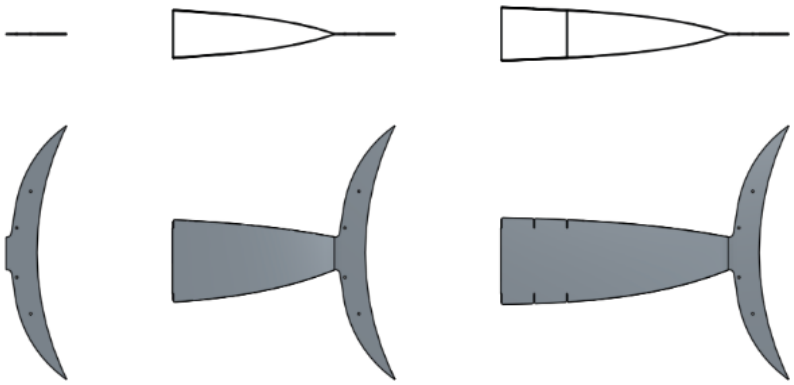

Figure 2.1: Plan and elevation views of zero, single, and dual-ribbed caudal fins

2.2 A Mechanical Model of a Caudal-Fin Actuator

A caudal fin actuator, illustrated in Figure 2.1, consists of a pair of thin curved beams joined at the distal end to attach a tail fin, which is bridged by rigid webs toward its proximal end. A proximal web is driven to induce large elastic oscillations of the

caudal-fin actuator to induce a thrust for an aquatic fish robot. To simulate the planar model-experiments in air that are driven by an oscillating proximal web (without distributed fluid interaction loading), finite element (FE) models are developed for caudal-fin actuators using three models: (a) without a web, (b) with one web, and (c) with two webs, as shown in Fig. 1. In FE models, thin flexible beams are modeled by using C^1 - beam elements based upon the Kirchhoff-Love beam theory [6] while rigid webs are modeled as rigid mass elements. (C^1- beam elements indicate that both beam deflection and it derivative with arc-parameter are continuous.) The FE equations of motion of the caudal-fin actuator, validated in air, may be utilized to evaluate the fluid interaction loading on the curved actuator walls by measuring their deformation in water. This approach mimics the inverse dynamics method employed in robotics.

In this report, the principle of virtual work is presented for the Kirchhoff-Love beam model for the first time. The principle of virtual work is utilized to develop FE beam elements, whose curve of centroids are expressed by continuous C^1-curves including the tangent to the curve at each FE node. In the presentation, it is crucial to clarify the effect of neglecting transverse shear deformation in the Kirchhoff-Love beam model and the resulting FE implementation of the zero-transverse shear constraint. Therefore, in the following, Reissner's shear-deformable beam equations [7] are fist derived from a free-body diagram, which includes the inertial terms. Then, the transverse shear deformation is neglected to reduce to the Kirchhoff-Love beam model, where the reactive-beam shear force is expressed by other beam stress variables. Afterward, starting from the principle of virtual work for Reissner's curved beam model obtained by the authors [8, 9], the principle of virtual work for the Kirchhoff-Love beam model is

derived. Finally, C^1-beam elements are introduced for the FE discretization of the principle of virtual work to obtain a nonlinear system of FE equations of motion, which is integrated with time by using the Newmark integration method [10, 11]

The application of FE models is confined in this report to capturing the nonlinear vibration of caudal-fin actuators in air. (The application of the FE equations of motion for inverse dynamics will be deferred to a future publication.)

2.3 Curved Beam Models and Their Assumptions

Plane beams carry internal axial force N_1 and transverse shear force N_2 (per unit length of the reference curve of centroids) as well as bending moment M_3 acting on each cross section, as illustrated in Fig. 2.2. Beams may be subjected to external transverse loading to the curved axis. To prepare for the derivation of beam equations of motion, the kinematic representation of curved beams is discussed first.

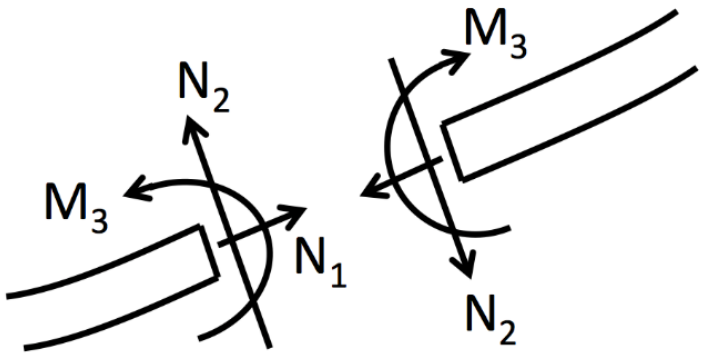

Figure 2.2: Plane beam showing internal axial force N_1, transverse shear force, N_2 and the bending moment M_3

2.3.1 Kinematics of Curved Beams

Let a plane beam deform in a Euclidean 2-space, spanned by an inertial Cartesian coordinate system $\{z_1 \quad z_2\}$ whose coordinate vector basis is: $\mathbf{e}^I \equiv \left(\mathbf{e}_1^I \quad \mathbf{e}_2^I\right)$. It is assumed that beam cross sections are symmetric with respect to the z_1, z_2-planes. The geometry of a beam in a reference or natural configuration at time t=0 is expressed as stacked cross sections with centroids that are joined by a curve of centroids, whose tangent is normal to each cross section. The *arc length* of the reference curve of centroids, $\mathbf{r}_C(S, 0)$, is expressed by S.

At time t, the deforming curve of centroids of cross sections, $\mathbf{r}_C(S, t)$, is parameterized by the *arc parameter S*, which was the arc length at the reference curve of centroids, $\mathbf{r}_C(S, 0)$. Using the coordinates, the position vector of the curve of centroids, $\mathbf{r}_C(S, t)$, at time t is expresses as

$$\mathbf{r}_C(S,t) = \mathbf{e}^I \, z_C(S,t) \equiv \left(\mathbf{e}_1^I \quad \mathbf{e}_2^I\right)\begin{pmatrix} z_{1C}(S,t) \\ z_{2C}(S,t) \end{pmatrix}. \tag{1}$$

Both Euler and James Bernoulli observed that for initially straight beams, each cross section does not deform in the plane of the cross section during deformation (*i.e.*, planar normal strains and shear strain are negligible), but rigidly translates and rotates, see Historical Introduction in Love's monograph [6]. The assumption of rigid cross sections was also adopted by Kirchhoff [12] and Love [6] for thin curved beams under large deformation. (Exceptional cases include, for example, a soft core sandwich beam or a beam with thin open channels which are not used for the side beams of the fin actuator.)

For a plane beam, a line defines each cross section, which is one of the principal axes of the cross section. At time t=0, each cross section, represented by a line, is normal to the reference curve of centroid. To define beam stress vectors and strains, as well as the rotation of cross sections at the arc-parameter S, an orthonormal vector basis: $\mathbf{e}(S,t) \equiv \left(\mathbf{e}_1(S,t) \quad \mathbf{e}_2(S,t)\right)$ is defined, where $\mathbf{e}_1(S,t)$ is the unit normal vector to the cross section and $\mathbf{e}_2(S,t)$ is the unit vector of the principal axis of the cross section at S, as illustrated in Fig. 2.3. The rotation angle $\psi(S,t)$ of the normal vector $\mathbf{e}_1(S,t)$ of cross section is measured from $\mathbf{e}_1^I$ in the counterclockwise direction (after parallel translating the inertial frame $\mathbf{e}^I \equiv \left(\mathbf{e}_1^I \quad \mathbf{e}_2^I\right)$ to $\mathbf{r}_C(S,t)$).

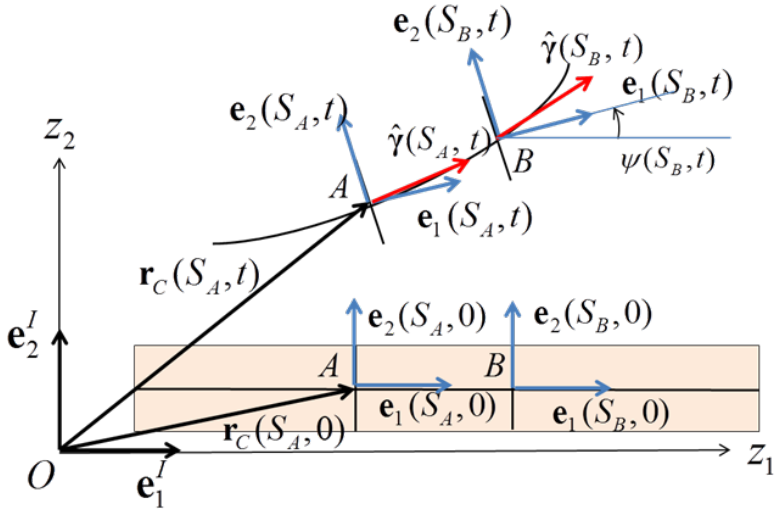

Figure 2.3: Beam section in the reference and actuated configuration

At t=0, $\mathbf{e}_1(S,0)$ is the unit tangent vector to the reference curve of centroids, $\mathbf{r}_C(S,0)$, and $\mathbf{e}_2(S,0)$ is the unit vector along one of the principal axes of the cross section. Since the cross section remains rigid, the normal strain in the $\mathbf{e}_2(S,t)$-direction vanishes.

However, due to transverse shear deformation, $\mathbf{e}_1(S,t)$ *may not remain tangent to the deforming curve of centroids*.

The attitude of $\mathbf{e}(S,t) \equiv \left(\mathbf{e}_1(S,t) \quad \mathbf{e}_2(S,t)\right)$, measured from the inertial frame $\mathbf{e}^I \equiv \left(\mathbf{e}_1^I \quad \mathbf{e}_2^I\right)$, is expressed symbolically by a rotation matrix $R(\psi(S,t))$ as:

$$\mathbf{e}(S,t) = \mathbf{e}^I R(\psi(S,t)), \tag{2a}$$

where the rotation matrix $R(\psi(S,t))$ by angle $\psi(S,t)$ in the counter clockwise direction is

$$R(\psi(S,t)) = \begin{bmatrix} \cos\psi(S,t) & -\sin\psi(S,t) \\ \sin\psi(S,t) & \cos\psi(S,t) \end{bmatrix}. \tag{2b}$$

In expanded form, Eq. (2a) is written as:

$$\left(\mathbf{e}_1(S,t) \quad \mathbf{e}_2(S,t)\right) = \left(\mathbf{e}_1^I \quad \mathbf{e}_2^I\right) \begin{bmatrix} \cos\psi(S,t) & -\sin\psi(S,t) \\ \sin\psi(S,t) & \cos\psi(S,t) \end{bmatrix}. \tag{2c}$$

Eq. (2a) may be interpreted as: "the moving frame $\mathbf{e}(S,t) \equiv \left(\mathbf{e}_1(S,t) \quad \mathbf{e}_2(S,t)\right)$ is obtained by rotating the inertial frame $\mathbf{e}^I \equiv \left(\mathbf{e}_1^I \quad \mathbf{e}_2^I\right)$ by $R(\psi(S,t))$." The inverse of the rotation matrix is expressed by its transpose as shown below:

$$R^{-1}(\psi(S,t)) = R(-\psi(S,t)) = \begin{bmatrix} \cos(-\psi(S,t)) & -\sin(-\psi(S,t)) \\ \sin(-\psi(S,t)) & \cos(-\psi(S,t)) \end{bmatrix}$$

$$= \begin{bmatrix} \cos\psi(S,t) & \sin\psi(S,t) \\ -\sin\psi(S,t) & \cos\psi(S,t) \end{bmatrix} \equiv R^T(\psi(S,t)).$$

Therefore, the inverse attitude relation to Eq. (2a) is expressed as:

$$\mathbf{e}^I = \mathbf{e}(S,t) R^T(\psi(S,t)). \tag{3}$$

The S-derivative of $\mathbf{e}(S,t)$ in Eq. (2a) expresses how the moving frame rotates as one moves along the curve of centroids. This relation takes a simple form when it is expressed by itself using Eq. (3).

$$\frac{\partial}{\partial S}\mathbf{e}(S,t) = \mathbf{e}^I \frac{\partial}{\partial S} R(\psi(S,t)) = \mathbf{e}(S,t) R^T(\psi(S,t)) \frac{\partial}{\partial S} R(\psi(S,t)).$$

The simple result gives

$$\frac{\partial}{\partial S}\mathbf{e}(S,t) = \mathbf{e}(S,t) \frac{\partial \psi(S,t)}{\partial S} \begin{bmatrix} 0 & -1 \\ 1 & 0 \end{bmatrix}, \tag{4a}$$

where

$$\frac{\partial \psi(S,t)}{\partial S} \begin{bmatrix} 0 & -1 \\ 1 & 0 \end{bmatrix} = R^T(\psi(S,t)) \frac{\partial}{\partial S} R(\psi(S,t)). \tag{4b}$$

Let the infinitesimal arc length be $ds = \sqrt{d\mathbf{r}_C \cdot d\mathbf{r}_C}$ of the current deformed curve of centroids, $\mathbf{r}_C(S,t)$, defined by the infinitesimal arc-parameter dS. Then, $\partial\psi/\partial s$ is the curvature of the moving frame $\mathbf{e}(S,t)$. As a result, $\partial\psi/\partial S = (\partial\psi/\partial s)(ds/dS)$ expresses the curvature of the moving frame, multiplied by the stretch ratio ds/dS. For initially curved beams, the initial curvature is expressed by $\partial\psi/\partial S$ since $ds/dS = 1$ at t=0.

Similarly, the time derivative of $\mathbf{e}(S,t)$ in Eq. (2a) shows the time-rate of frame rotation whose amplitude is expressed by angular velocity $\partial\psi/\partial t$. Again, the expression takes a simple form when it is expressed by itself using Eq. (3).

$$\frac{\partial}{\partial t}\mathbf{e}(S,t) = \mathbf{e}^I \frac{\partial}{\partial t} R(\psi(S,t)) = \mathbf{e}(S,t) R^T(\psi(S,t)) \frac{\partial}{\partial t} R(\psi(S,t)).$$

The result gives

$$\frac{\partial}{\partial t}\mathbf{e}(S,t) = \mathbf{e}(S,t) \frac{\partial \psi(S,t)}{\partial t} \begin{bmatrix} 0 & -1 \\ 1 & 0 \end{bmatrix}, \tag{5a}$$

where

$$\frac{\partial \psi(S,t)}{\partial t}\begin{bmatrix} 0 & -1 \\ 1 & 0 \end{bmatrix} = R^T(\psi(S,t))\frac{\partial}{\partial t}R(\psi(S,t)). \tag{5b}$$

Geometrically, the curve of centroids with an orthonormal vector basis, $\mathbf{e}(S,t)$, attached at each point, forms a *frame bundle* [13]. As a result, the deformed configuration of a beam is described by three coordinates or displacements: $\{z_{1C}(S,t) \quad z_{2C}(S,t) \quad \psi(S,t)\}$, as illustrated in Fig. 2.3. These displacement functions are continuous and differentiable with respect to both the arc-parameter S and time t. Let the tangent vector to the current curve of centroid be denoted by $\hat{\boldsymbol{\gamma}}(S,t)$:

$$\hat{\boldsymbol{\gamma}}(S,t) \equiv \frac{\partial \mathbf{r}_C}{\partial S}(S,t) = \mathbf{e}^1 \frac{\partial z_C}{\partial S} \equiv \begin{pmatrix} \mathbf{e}_1^1 & \mathbf{e}_2^1 \end{pmatrix}\begin{pmatrix} \dfrac{\partial z_{1C}}{\partial S} \\ \dfrac{\partial z_{2C}}{\partial S} \end{pmatrix}. \tag{6a}$$

The components of the tangent vector $\hat{\boldsymbol{\gamma}}(S,t)$ is also expressed by the moving frame $\mathbf{e}(S,t)$ as

$$\hat{\boldsymbol{\gamma}}(S,t) = \mathbf{e}(S,t)\hat{\gamma}(S,t) \equiv \begin{pmatrix} \mathbf{e}_1(S,t) & \mathbf{e}_2(S,t) \end{pmatrix}\begin{pmatrix} \hat{\gamma}_1(S,t) \\ \hat{\gamma}_2(S,t) \end{pmatrix}. \tag{6b}$$

In general, the unit normal $\mathbf{e}_1(S,t)$ of cross section is not parallel to the tangent $\hat{\boldsymbol{\gamma}}(S,t)$ to the deformed curve of centroids, $\mathbf{r}_C(S,t)$:

$$\psi(S,t) \neq \tan^{-1}\left(\frac{\dfrac{\partial z_{2C}}{\partial S}}{\dfrac{\partial z_{1C}}{\partial S}}\right). \tag{7}$$

In Eq. (6b), $\hat{\gamma}_1(S,t)$ shows the stretch ratio in the normal direction of cross section. The term $\hat{\gamma}_2(S,t)$ indicates the *transverse shear strain*, indicating that the angle reduction between $\mathbf{e}_2(S,t)$, and $\hat{\boldsymbol{\gamma}}(S,t)$ from $\pi/2$ [8].

For thin straight beams under small deformation, both Euler and Bernoulli [14] observed that each cross-section normal to the line of centroids remains normal during deformation. The observation indicates that $\hat{\gamma}_2(S,t) \approx 0$. Their beam model, incorporating $\hat{\gamma}_2(S,t) = 0$, is known as the *Euler-Bernoulli beam* model, which is presented in the Appendix.

For curved beams, both Kirchhoff [12] and Love [6] observed that the normality assumption of cross sections during beam deformation, $\hat{\gamma}_2(S,t) \approx 0$, also applies to curved thin beams under large deformation. Their curved beam model is known as the *Kirchhoff-Love beam* model. Since the unit normal $\mathbf{e}_1(S,t)$ of cross section remains parallel to the tangent vector $\hat{\boldsymbol{\gamma}}(S,t)$ to the curve of centroids, $\mathbf{r}_C(S,t)$, the tangent vector for the Kirchhoff-Love beam model becomes:

$$\hat{\boldsymbol{\gamma}}(S,t) = \hat{\gamma}_1(S,t)\mathbf{e}_1(S,t) \text{ and } \hat{\gamma}_2(S,t) = 0. \tag{8a, b}$$

The angular displacement $\psi(S,t)$ of the cross section at S is expressed by the S-derivatives of $z_C(S,t)$ in Eq. (1) for the Kirchhoff-Love beam model as:

$$\psi(S,t) = \tan^{-1}\left(\frac{\dfrac{\partial z_{2C}}{\partial S}}{\dfrac{\partial z_{1C}}{\partial S}}\right). \tag{8c}$$

As a result of the constraint, $\hat{\gamma}_2(S,t) = 0$, the deformed configuration of a beam is described by using only the S-derivatives of the two coordinates or displacements, $z_C(S,t)$

. This reduction of independent displacement fields leads to simpler equilibrium equations for analytical solutions and a smaller number of total nodal displacements in a nonlinear FE model.

Following Reissner [15], in the next section, the equations of motion for curved beams are derived, including axial and transverse shear deformation, which were neglected in the earlier curved beam models. Subsequently, Reissner's curved beam equations will be specialized for the Kirchhoff-Love beams introducing the constraint, $\hat{\gamma}_2(S,t) = 0$, to clarify the effect of reactive shear force.

The current presentation of various beam models is in reverse chronological order, to expediently present the principle of virtual work, which is essential for the development of FE beam models, with a focus on the Kirchhoff-Love beam theory. Unfortunately, earlier beam models were obtained by introducing as many legitimate assumptions as possible to obtain analytical solutions since computational tools such as FE analyses were not available in the 19th century and the first half of the 20th century. Therefore, alternative weak form presentations of the earlier beam models, such as the principle of virtual work, were not presented for numerical computations.

2.3.2 Derivation of Reissner's Curved-Beam Equations

Beam stress vector $\mathbf{N}(S,t)$ represents the normal force $N_1(S,t)$ and the *transverse shear force* $N_2(S,t)$ per unit length of the reference curve of centroids:

$$\mathbf{N}(S,t) = \mathbf{e}(S,t)\begin{pmatrix} N_1(S,t) \\ N_2(S,t) \end{pmatrix}. \tag{9}$$

The bending moment acting on the cross section at S on the deformed curve of centroids, $\mathbf{r}_C(S,t)$, is denoted by $M_3(S,t)$.

To represent the effect of gravitational body force and distributed surface tractions, external distributed force $\hat{\mathbf{n}}(S,t)$ and distributed couple $\hat{m}_3(S,t)$ are also considered along the curve of centroids. The components of the distributed force $\hat{\mathbf{n}}(S,t)$ are expressed with the moving frame as:

$$\hat{\mathbf{n}}(S,t) = \mathbf{e}(S,t)\begin{pmatrix}\hat{n}_1(S,t)\\ \hat{n}_2(S,t)\end{pmatrix}. \tag{10}$$

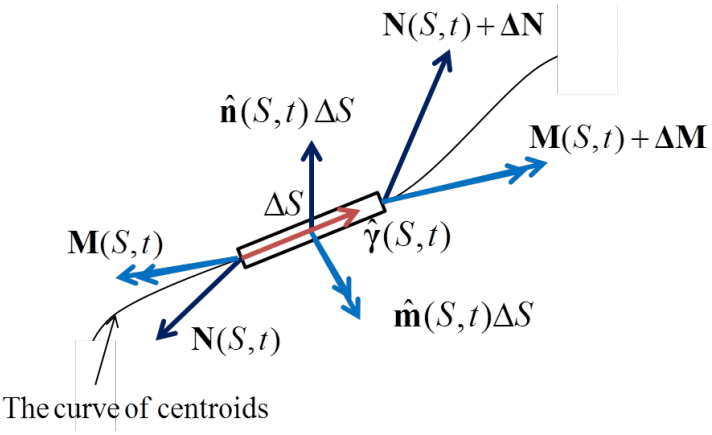

Figure 2.4: A free body diagram of a beam element with the arc-parameter increment of DS

To acquire a geometrical picture, a free-body diagram of an infinitesimal beam element is shown, between the arc parameter S and $S+\Delta S$ in Fig. 2.4. The element is subjected to the beam stress vector $\mathbf{N}(S,t)$, moment $M_3(S,t)$, the distributed force $\hat{\mathbf{n}}(S,t)$, and distributed couple $\hat{m}_3(S,t)$. In the figure, the tangent vector $\hat{\gamma}(S,t)$ to the deformed curve of centroids is also shown.

The free-body-diagram was originally employed by Reissner to derive equilibrium equations [7]. By adding inertial forces, the same diagram enables the derivation of the equations of motion for the dynamic loading.

Let the mass per unit length of the reference curve of centroids be expressed by $\mathsf{m}_{A(0),}$. For translational motion Newton's second law applies:

$$\lim_{\Delta S\to 0}\frac{1}{\Delta S}\left(\Delta\mathbf{N}(S,t)+\hat{\mathbf{n}}(S,t)\Delta S-\mathsf{m}_{A(0)}\Delta S\frac{\partial^2}{\partial t^2}\mathbf{r}_C(S,t)\right)=0. \tag{11a}$$

For the rotational motion of the cross section, time rate of angular momentum becomes the external torque applied to the element, according to Euler. Let the mass moment of inertial of the cross section be denoted by $J_{3C(0)}$. The free-body-diagram, considering the moment with the z_3-axis, normal to the z_1, z_2 planes, one obtains

$$\lim_{\Delta S\to 0}\frac{1}{\Delta S}\left(\Delta M_3(S,t)+(\hat{\boldsymbol{\gamma}}(S,t)\Delta S\times\mathbf{N}(S,t))_3+\hat{m}_3(S,t)\Delta S-J_{3C(0)}\Delta S\frac{\partial^2}{\partial t^2}\psi(S,t)\right)=0. \tag{11b}$$

The cross product in Eq. (11b) with respect to $\mathbf{e}(S,t)$ is evaluated using Eqs. (6b) and (9) and find

$$(\hat{\boldsymbol{\gamma}}(S,t)\Delta S\times\mathbf{N}(S,t))_3=\Delta S\left\{-\hat{\gamma}_2(S,t)N_1(S,t)+\hat{\gamma}_1(S,t)N_2(S,t)\right\}. \tag{11c}$$

From Eq. (11a), the beam equations of motion for translational motion is

$$\frac{\partial}{\partial S}\mathbf{N}(S,t)+\hat{\mathbf{n}}(S,t)=\mathsf{m}_{A(0)}\frac{\partial^2}{\partial t^2}\mathbf{r}_C(S,t). \tag{12}$$

From Eqs. (11b, c), the beam rotational equation of motion becomes

$$\frac{\partial}{\partial S}M_3(S,t)-\hat{\gamma}_2(S,t)N_1(S,t)+\hat{\gamma}_1(S,t)N_2(S,t)+\hat{m}_3(S,t)=J_{3C(0)}\frac{\partial^2}{\partial t^2}\psi(S,t). \tag{13}$$

The component expression of Eq. (12) is obtained by substituting Eqs. (9) and (10) into the left-hand side and using Eq. (4):

$$LHS = \frac{\partial}{\partial S}\left(\mathbf{e}\,N\right) + \mathbf{e}\,\hat{n} = \frac{\partial \mathbf{e}}{\partial S}N + \mathbf{e}\frac{\partial N}{\partial S} + \mathbf{e}\,\hat{n}$$

$$= \mathbf{e}\left(\frac{\partial \psi}{\partial S}\begin{bmatrix}0 & -1\\ 1 & 0\end{bmatrix}\begin{pmatrix}N_1\\ N_2\end{pmatrix} + \frac{\partial}{\partial S}\begin{pmatrix}N_1\\ N_2\end{pmatrix} + \begin{pmatrix}\hat{n}_1\\ \hat{n}_2\end{pmatrix}\right), \tag{14a}$$

The right-hand side of Eq. (12) is computed by taking the time derivative of Eq. (1) twice as:

$$RHS = \mathbf{e}^I\,\mathsf{m}_{\mathsf{A}(0)}\frac{\partial^2 z_C}{\partial t^2}. \tag{14b}$$

The resulting translational equations of motion are expressed with respect to the inertial frame as follows:

$$\begin{bmatrix}\cos\psi(S,t) & -\sin\psi(S,t)\\ \sin\psi(S,t) & \cos\psi(S,t)\end{bmatrix}\begin{pmatrix}\frac{\partial}{\partial S}N_1(S,t) - \frac{\partial\psi(S,t)}{\partial S}N_2(S,t) + \hat{n}_1(S,t)\\ \frac{\partial}{\partial S}N_2(S,t) + \frac{\partial\psi(S,t)}{\partial S}N_1(S,t) + \hat{n}_2(S,t)\end{pmatrix}$$

$$= \begin{pmatrix}\mathsf{m}_{\mathsf{A}(0)}\frac{\partial^2 z_{1C}(S,t)}{\partial t^2}\\ \mathsf{m}_{\mathsf{A}(0)}\frac{\partial^2 z_{2C}(S,t)}{\partial t^2}\end{pmatrix}. \tag{15}$$

For static problems, Eqs. (12), (13), and (15) reduce to the equilibrium equations presented by Reissner [7]. Although Reissner left the moving frame be undefined, it was identified to be the moving frame defined in this report [8,9].

For elastic beams under large deformation, but small strains, Hooke's law relates the beam axial force, shear force, and bending moment (per unit reference line of centroids) to axial strain, $\hat{\gamma}_1 - 1$, shear strain, $\hat{\gamma}_2$, and the relative curvature, $\partial\psi/\partial S(S,t) - \partial\psi/\partial S(S,0)$,

respectively. For a homogeneous beam with Young's modulus E, shear modulus G, area of cross section A, and areal moment of inertia I_3, Hooke's law yields

$$N_1(S,t) = EA\left(\hat{\gamma}_1(S,t) - 1\right), \tag{16a}$$

$$N_2(S,t) = GA_s\,\hat{\gamma}_2(S,t), \tag{16b}$$

$$M_3(S,t) = EI_3\left(\frac{\partial}{\partial S}\psi(S,t) - \frac{\partial}{\partial S}\psi(S,0)\right), \tag{16c}$$

where A_s is the area of cross section for shear deformation (to incorporate the shear correction factor). For a rectangular cross section, a shear correction factor of 5/6 is used after Reissner [9]

In summary, the large deformation of an initially curved beam under small strain is described by the equations of motion, Eqs. (15) and (13) , Hooke's law, Eqs. (16a-c), the definition of the tangent vector $\hat{\boldsymbol{\gamma}}(S,t)$ in Eqs. (6a, b), and the evolution of moving frames $\mathbf{e}(S,t)$ with respect to S, Eq. (4) and with respect to t, Eq. (5), both of which define the attitude of the moving frame, Eq. (2a).

Next, the principle of virtual work associated with the above beam equations is presented. Considering virtual displacement of the curve of centroids $\delta\mathbf{r}_C(S,t)$ and the virtual angular displacement $\delta\psi(S,t)$, where

$$\delta\mathbf{r}_C(S,t) = \mathbf{e}^I\,\delta z_C(S,t) \equiv \begin{pmatrix}\mathbf{e}_1^I & \mathbf{e}_2^I\end{pmatrix}\begin{pmatrix}\delta z_{1C}(S,t)\\ \delta z_{2C}(S,t)\end{pmatrix}. \tag{17}$$

The principle of virtual work, which yields Eqs. (15) and (13) as the Euler-Lagrange equations, has already been presented [3,4]:

$$\int_0^L \left\{ \begin{pmatrix} \delta\hat{\gamma}_1(S,t) & \delta\hat{\gamma}_2(S,t) \end{pmatrix} \begin{pmatrix} N_1(S,t) \\ N_2(S,t) \end{pmatrix} + \delta\left(\frac{\partial \psi(S,t)}{\partial S} \right) M_3(S,t) \right\} dS$$

$$= \int_0^L \left\{ \delta\mathbf{r}_C(S,t) \cdot \left(\hat{\mathbf{n}}(S,t) - \mathsf{m}_{\mathsf{A}(0)} \frac{\partial^2 \mathbf{r}_C(S,t)}{\partial t^2} \right) \right.$$

$$\left. + \delta\psi(S,t) \left(\hat{m}_3(S,t) - J_{3C(0)} \frac{\partial^2 \psi(S,t)}{\partial t^2} \right) \right\} dS$$

$$+ \left\{ \delta\mathbf{r}_C(S,t) \cdot \hat{\mathbf{n}}_E(S,t) + \delta\psi(S,t) \hat{m}_E(S,t) \right\}_{S=0}^{S=L} . \qquad (18)$$

The left-hand side represents the virtual strain energy of the beam, induced by the resultant stress vector $\mathbf{N}(S,t)$ working on the components of virtual normal and shear strains and moment $M_3(S,t)$ on the virtual angular displacement.

On the right-hand side of Eq. (18), the two integrals show, respectively, the virtual work done by the distributed load $\hat{\mathbf{n}}(S,t)$ and the inertial force on the virtual displacements $\delta\mathbf{r}_C(S,t)$ and the virtual work of the distributed torque $\hat{m}_3(S,t)$ and the inertial torque on the virtual angular displacement $\delta\psi(S,t)$. The terms in the last pair of braces are virtual work done by the boundary force $\hat{\mathbf{n}}_E$ on the boundary virtual displacement $\delta\mathbf{r}_C$ and the boundary couple $\hat{m}_E$ on the boundary virtual angular displacement $\delta\psi$. Since there are three displacements including the angular displacement, at each boundary, two traction components and moment can be prescribed.

In the Kirchhoff-Love beam model, the transverse shear deformation is neglected, $\hat{\gamma}_2(S,t) = 0$, as a result, beam displacements reduce two (without angular displacement). Therefore, the virtual angular displacement $\delta\psi$ must be expressed by the virtual displacements and their S-derivatives. In the next section, the Kirchhoff-Love beam

equations are obtained by imposing $\hat{\gamma}_2 = 0$ on Reissner's curved beam equations, Eq. (15) and (13).

2.3.3 Reduction to the Kirchhoff-Love Beam Equations

The constraint, $\hat{\gamma}_2 = 0$ in Eq. (8a) makes the shear force constitutive equation, Eq. (16b), invalid. Observing that nonzero shear force exists in deforming beams regardless of the constraint $\hat{\gamma}_2 = 0$, Eq. (16b) only makes sense at the simultaneous limits of $GA_s \to \infty$ and $\hat{\gamma}_2 \to 0$. This indicates that shear force become a *reactive force*, for which the shear constitutive relation, Eq. (16b), does not hold, (but equilibrium equations and equations of motion hold).

For thin beams, both transverse shear strain, $\hat{\gamma}_2$, and the mass moment of inertia, J_{3C}, become negligible. Further, neglecting the distributed couple $\hat{m}_3$ in Eq. (13), the shear force $N_2(S,t)$ is expressed as:

$$N_2(S,t) = -\frac{1}{\hat{\gamma}_1(S,t)}\left(\frac{\partial}{\partial S} M_3(S,t)\right). \tag{19}$$

The definition of the tangent vector to the curve of centroids, $\hat{\boldsymbol{\gamma}}(S,t)$, in Eqs. (6a, b) with $\hat{\gamma}_2 = 0$, indicates $\hat{\boldsymbol{\gamma}}(S,t) = \hat{\gamma}_1(S,t)\mathbf{e}_1(S,t)$.

$$\hat{\gamma}_1(S,t) = \left\| \hat{\boldsymbol{\gamma}}(S,t) \right\| \equiv \sqrt{\left(\frac{\partial z_C}{\partial S}\right)^T \left(\frac{\partial z_C}{\partial S}\right)} \equiv \sqrt{\left(\frac{\partial z_{1C}}{\partial S}\right)^2 + \left(\frac{\partial z_{2C}}{\partial S}\right)^2}. \tag{20a}$$

The direction cosine of $\hat{\boldsymbol{\gamma}}(S,t)$ is from Eq. (6a)

$$\begin{pmatrix}\cos\psi(S,t)\\ \sin\psi(S,t)\end{pmatrix} = \frac{1}{\hat{\gamma}_1(S,t)}\frac{\partial z_C(S,t)}{\partial S} \equiv \frac{1}{\hat{\gamma}_1(S,t)}\begin{pmatrix}\dfrac{\partial z_{1C}(S,t)}{\partial S}\\ \dfrac{\partial z_{2C}(S,t)}{\partial S}\end{pmatrix}, \tag{20b}$$

which may be written, when $\partial z_{1C}/\partial S$ does not vanish as:

$$\psi(S,t) = \tan^{-1}\left(\frac{\partial z_{2C}/\partial S}{\partial z_{1C}/\partial S}\right). \tag{20c}$$

Let *ds* be the infinitesimal arc length of the deformed curve of centroids, which corresponds to *dS* on the reference curve of centroids, $\mathbf{r}_C(S,0)$. Then, axial strain $\hat{\gamma}_1$ expresses a stretch ratio $\hat{\gamma}_1 = ds/dS$. Therefore, if the arc-length *ds* on the current curve of centroids were used, Eq. (19) could be written as: $N_2(S,t) = -\partial M_3(S,t)/\partial s$. (Since the arc length *s* changes each time, it is easier to deal with the arc-parameter *S* in FE analyses.)

Using Eq. (19) in Eq. (15), the equations of motion for the Kirchhoff-Love beam model are obtained:

$$\begin{bmatrix}\cos\psi(S,t) & -\sin\psi(S,t)\\ \sin\psi(S,t) & \cos\psi(S,t)\end{bmatrix}\begin{pmatrix}\dfrac{\partial}{\partial S}N_1(S,t) + \dfrac{\partial\psi(S,t)}{\partial S}\left(\dfrac{1}{\hat{\gamma}_1(S,t)}\dfrac{\partial}{\partial S}M_3(S,t)\right) + \hat{n}_1(S,t)\\ -\dfrac{\partial}{\partial S}\left(\dfrac{1}{\hat{\gamma}_1(S,t)}\dfrac{\partial}{\partial S}M_3(S,t)\right) + \dfrac{\partial\psi(S,t)}{\partial S}N_1(S,t) + \hat{n}_2(S,t)\end{pmatrix} =$$

$$= \begin{pmatrix}\mathsf{m}_{A(0)}\dfrac{\partial^2 z_{1C}(S,t)}{\partial t^2}\\ \mathsf{m}_{A(0)}\dfrac{\partial^2 z_{2C}(S,t)}{\partial t^2}\end{pmatrix}. \tag{21}$$

For static problems, Eq. (21) agrees with the planar equilibrium equations presented by Love [1].

In Eq. (21), only $N_1(S,t)$ and $M_3(S,t)$ appear. Next, their constitutive relations are considered. Eq. (16a) holds for $N_1(S,t)$. However, in the moment constitutive relation, Eq.

(16c), the relative curvature term: $\partial\psi/\partial S(S,t) - \partial\psi/\partial S(S,0)$ must be rewritten imposing $\hat{\gamma}_2 = 0$.

Equations (6a) and (6b) expressed with the moving frame $\mathbf{e}(S,t)$ yield

$$\begin{pmatrix} \hat{\gamma}_1(S,t) \\ 0 \end{pmatrix} = \begin{bmatrix} \cos\psi(S,t) & \sin\psi(S,t) \\ -\sin\psi(S,t) & \cos\psi(S,t) \end{bmatrix} \begin{pmatrix} \partial z_{1C}/\partial S \\ \partial z_{2C}/\partial S \end{pmatrix}. \tag{22}$$

By taking the S-derivative of the first row of Eq. (22) and using the second row, $\partial\hat{\gamma}_1/\partial S$ is expressed by the S-derivatives of $z_{1C}(S,t)$ and $z_{2C}(S,t)$ as:

$$\frac{\partial\hat{\gamma}_1(S,t)}{\partial S} = \begin{bmatrix} \cos\psi(S,t) & \sin\psi(S,t) \end{bmatrix} \begin{pmatrix} \partial^2 z_C(S,t)/\partial S^2 \end{pmatrix}. \tag{23}$$

By taking the S-derivative of the second row of Eq. (22) and using the first row, $\partial\psi/\partial S$ is expressed by the S-derivatives of $z_{1C}(S,t)$ and $z_{2C}(S,t)$ as:

$$\frac{\partial\psi(S,t)}{\partial S} = \frac{1}{\hat{\gamma}_1(S,t)} \begin{bmatrix} -\sin\psi(S,t) & \cos\psi(S,t) \end{bmatrix} \begin{pmatrix} \partial^2 z_C(S,t)/\partial S^2 \end{pmatrix}, \tag{24a}$$

where the following compact notation is employed:

$$\begin{pmatrix} \partial^2 z_C(S,t)/\partial S^2 \end{pmatrix} \equiv \begin{pmatrix} \partial^2 z_{1C}(S,t)/\partial S^2 \\ \partial^2 z_{2C}(S,t)/\partial S^2 \end{pmatrix}. \tag{24b}$$

The initial curvature is, observing that $\hat{\gamma}_1(S,0) = 1$:

$$\frac{\partial\psi(S,0)}{\partial S} = \begin{bmatrix} -\sin\psi(S,0) & \cos\psi(S,0) \end{bmatrix} \begin{pmatrix} \partial^2 z_C(S,0)/\partial S^2 \end{pmatrix}. \tag{25}$$

Using Eqs. (24a) and (25) for the relative curvature terms in Eq. (16c), the moment constitutive relation becomes:

$$M_3(S,t) = E I_3 \left\{ \begin{array}{l} \dfrac{1}{\hat{\gamma}_1(S,t)} \left[-\sin\psi(S,t) \quad \cos\psi(S,t) \right] \left(\dfrac{\partial^2 z_C(S,t)}{\partial S^2} \right) \\ -\left[-\sin\psi(S,0) \quad \cos\psi(S,0) \right] \left(\dfrac{\partial^2 z_C(S,0)}{\partial S^2} \right) \end{array} \right\}. \tag{26}$$

In summary, the Kirchhoff-Love planar beam equations consist of the following: (i) equations of motion, Eq. (21) for $z_{1C}(S,t)$ and $z_{2C}(S,t)$, and (ii) the constitutive relations for $N_1(S,t)$, Eq. (16a), and $M_3(S,t)$, Eq. (26). The shear force (per unit reference curve of centroids) becomes a reactive stress variable and is computed using Eq. (19) after $M_3(S,t)$ is found. In those equations, $\hat{\gamma}_1(S,t)$, $\cos\psi(S,t)$, and $\sin\psi(S,t)$ are expressed by the *S*-derivatives of $z_{1C}(S,t)$ and $z_{2C}(S,t)$, using Eq. (20a-c).

2.3.4 The Principle of Virtual Work for the Kirchhoff-Love Beams

The principle of virtual work facilitates a guiding equation for the development of nonlinear FE codes for the Kirchhoff-Love beams. The principle is obtained from Eq. (18) by incorporating the same assumptions: (i) zero transverse shear strain, $\hat{\gamma}_2 = 0$, zero mass moment of inertia of cross section, $J_{3C(0)} = 0$, and zero distributed couple, $\hat{m}_3 = 0$, which were utilized to reduce the Kirchhoff-Love equations from Reissner's curved beam equations. Due to $\hat{\gamma}_2 = 0$, $\delta\psi(S,t)$ will depend on the *S*-derivatives of $\delta z_{1C}(S,t)$ and $\delta z_{2C}(S,t)$. The resulting principle of virtual work for the Kirchhoff-Love beams is obtained from Eq. (18) as:

$$\int_0^L \left\{ \delta\hat{\gamma}_1(S,t) N_1(S,t) + \delta\left(\frac{\partial\psi(S,t)}{\partial S} \right) M_3(S,t) \right\} dS$$

$$= \int_0^L \left\{ \delta \mathbf{r}_C(S,t) \cdot \left(\hat{\mathbf{n}}(S,t) - \mathsf{m}_{A(0)} \frac{\partial^2 \mathbf{r}_C(S,t)}{\partial t^2} \right) \right\} dS$$

$$+ \left[\delta \mathbf{r}_C(S,t) \cdot \hat{\mathbf{n}}_E(S,t) + \delta\psi(S,t)\, \hat{m}_E(S,t) \right|_{S=0}^{S=L}. \qquad (27)$$

For arbitrary variations of $\delta z_{1C}(S,t)$ and $\delta z_{2C}(S,t)$, the Euler-Lagrange equations of Eq. (27) must yield Eq. (21). As a by-product, in the computation of the Euler-Lagrange equations, "variationally consistent" boundary conditions will be obtained.

2.3.5 The Euler-Lagrange Equations

First, the beam virtual strain energy term is rewritten by expressing the virtual axial strain $\delta\hat{\gamma}_1(S,t)$ and the virtual curvature $\partial\delta\psi(S,t)/\partial S$ in terms of the S-derivatives of $\delta z_{1C}(S,t)$ and $\delta z_{2C}(S,t)$. In the computations, one observes that the variational δ-operator and the S-differential operator commute, such as $\delta(\partial\psi(S,t)/\partial S) = \partial\delta\psi(S,t)/\partial S$. Since the Kirchhoff-Love beam equations have not been derived from the principle of virtual work, the computational steps of the derivation are presented in what follows.

The virtual axial strain $\delta\hat{\gamma}_1(S,t)$ is computed by taking the variation of the first row of Eq. (22) and using the second row as:

$$\delta\hat{\gamma}_1(S,t) = \left[\cos\psi(S,t) \quad \sin\psi(S,t) \right] \left(\frac{\partial \delta z_C(S,t)}{\partial S} \right), \qquad (28a)$$

where the following compact notation is used:

$$\left(\frac{\partial \delta z_C(S,t)}{\partial S} \right) \equiv \begin{pmatrix} \dfrac{\partial \delta z_{1C}(S,t)}{\partial S} \\ \dfrac{\partial \delta z_{2C}(S,t)}{\partial S} \end{pmatrix}. \qquad (28b)$$

Next, taking the variation of the second row of Eq. (22) and using its first row, $\delta\psi(S,t)$ is expressed by $\partial\delta z_C/\partial S$ and the direction cosines, which are expressed by $\partial z_C/\partial S$ in Eq. (21b, c):

$$\delta\psi(S,t)=\frac{1}{\hat{\gamma}_1(S,t)}\left[-\sin\psi(S,t)\quad\cos\psi(S,t)\right]\left(\frac{\partial\delta z_C(S,t)}{\partial S}\right). \tag{29}$$

The S-derivative of Eq. (29) becomes

$$\frac{\partial\delta\psi(S,t)}{\partial S}=\left\{\frac{1}{\hat{\gamma}_1(S,t)}\left[-\sin\psi(S,t)\quad\cos\psi(S,t)\right]\right\}\left(\frac{\partial^2\delta z_C(S,t)}{\partial S^2}\right)$$

$$+\frac{\partial}{\partial S}\left\{\frac{1}{\hat{\gamma}_1(S,t)}\left[-\sin\psi(S,t)\quad\cos\psi(S,t)\right]\right\}\left(\frac{\partial\delta z_C(S,t)}{\partial S}\right), \tag{30a}$$

where the following compact notation is employed:

$$\left(\frac{\partial^2\delta z_C(S,t)}{\partial S^2}\right)\equiv\begin{pmatrix}\dfrac{\partial^2\delta z_{1C}(S,t)}{\partial S^2}\\[2ex]\dfrac{\partial^2\delta z_{2C}(S,t)}{\partial S^2}\end{pmatrix}. \tag{30b}$$

The left-hand side of Eq. (27) expresses the virtual strain energy of the beam. This integral is rewritten using Eqs. (28a) and (30a) as:

$$LHS=\int_0^L\left[\left(\frac{\partial\delta z_C}{\partial S}\right)^T\left\{\begin{bmatrix}\cos\psi\\\sin\psi\end{bmatrix}N_1+\frac{\partial}{\partial S}\left(\frac{1}{\hat{\gamma}_1}\begin{bmatrix}-\sin\psi\\\cos\psi\end{bmatrix}\right)M_3\right\}+\left(\frac{\partial^2\delta z_C}{\partial S^2}\right)^T\frac{1}{\hat{\gamma}_1}\begin{bmatrix}-\sin\psi\\\cos\psi\end{bmatrix}M_3\right]dS. \tag{31a}$$

The integration by parts is repeated until all the S-derivatives of δz_C are removed:

$$\begin{aligned}LHS=&\left[(\delta z_C)^T\left\{\begin{bmatrix}\cos\psi\\\sin\psi\end{bmatrix}N_1+\frac{\partial}{\partial S}\left(\frac{1}{\hat{\gamma}_1}\begin{bmatrix}-\sin\psi\\\cos\psi\end{bmatrix}\right)M_3\right\}\right|_{S=0}^{S=L}+\left[\left(\frac{\partial\delta z_C}{\partial S}\right)\frac{1}{\hat{\gamma}_1}\begin{bmatrix}-\sin\psi\\\cos\psi\end{bmatrix}M_3\right|_{s+0}^{S=L}\\&-\int_0^L\left[(\delta z_C)^T\frac{\partial}{\partial S}\left\{\begin{bmatrix}\cos\psi\\\sin\psi\end{bmatrix}N_1+\frac{\partial}{\partial S}\left(\frac{1}{\hat{\gamma}_1}\begin{bmatrix}-\sin\psi\\\cos\psi\end{bmatrix}\right)M_3\right\}+\left(\frac{\partial\delta z_C}{\partial S}\right)^T\frac{\partial}{\partial S}\left(\frac{1}{\hat{\gamma}_1}\begin{bmatrix}-\sin\psi\\\cos\psi\end{bmatrix}M_3\right)\right]dS\end{aligned}, \tag{31b}$$

Another integration by part is applied to the last term in the integrand and simple computations yield:

$$LHS = \left[(\delta z_C)^T \left\{ \begin{bmatrix} \cos\psi \\ \sin\psi \end{bmatrix} N_1 - \begin{bmatrix} -\sin\psi \\ \cos\psi \end{bmatrix} \frac{1}{\hat{\gamma}_1} \frac{\partial M_3}{\partial S} \right\} \right|_{s=0}^{S=L} + \left[\left(\frac{\partial \delta z_C}{\partial S} \right) \begin{bmatrix} -\sin\psi \\ \cos\psi \end{bmatrix} \frac{1}{\hat{\gamma}_1} M_3 \right|_{s+0}^{S=L} \quad (31c)$$
$$- \int_0^L \left[(\delta z_C)^T \frac{\partial}{\partial S} \left\{ \begin{bmatrix} \cos\psi \\ \sin\psi \end{bmatrix} N_1 - \begin{bmatrix} -\sin\psi \\ \cos\psi \end{bmatrix} \frac{1}{\hat{\gamma}_1} \frac{\partial M_3}{\partial S} \right\} \right] dS$$

Finally, Eq. (31c) is rewritten using the rotation matrix defined in Eq. (2b) as:

$$LHS = \left[(\delta z_C)^T R(\psi(S,t) \left(\begin{matrix} N_1 \\ -\frac{1}{\hat{\gamma}_1} \frac{\partial M_3}{\partial S} \end{matrix} \right) \right|_{s=0}^{S=L} + \left[\left(\frac{\partial \delta z_C}{\partial S} \right) \begin{bmatrix} -\sin\psi \\ \cos\psi \end{bmatrix} \frac{1}{\hat{\gamma}_1} M_3 \right|_{s+0}^{S=L}$$

$$- \int_0^L \left[(\delta z_C)^T \frac{\partial}{\partial S} \left\{ R(\psi(S,t) \left(\begin{matrix} N_1 \\ -\frac{1}{\hat{\gamma}_1} \frac{\partial M_3}{\partial S} \end{matrix} \right) \right\} \right] dS \quad . \quad (31d)$$

The integrand of the equation above is evaluated using Eq. (4b) as

$$LHS = \left[(\delta z_C)^T R(\psi(S,t) \left(\begin{matrix} N_1 \\ -\frac{1}{\hat{\gamma}_1} \frac{\partial M_3}{\partial S} \end{matrix} \right) \right|_{s=0}^{S=L} + \left[\left(\delta \frac{\partial z_C}{\partial S} \right)^T \begin{bmatrix} -\sin\psi \\ \cos\psi \end{bmatrix} \frac{1}{\hat{\gamma}_1} M_3 \right|_{s+0}^{S=L}$$
$$- \int_0^L (\delta z_C(S,t))^T R(\psi(S,t) \left\{ \frac{\partial}{\partial S} \left(\begin{matrix} N_1 \\ -\frac{1}{\hat{\gamma}_1} \frac{\partial M_3}{\partial S} \end{matrix} \right) + \frac{\partial \psi}{\partial S} \begin{bmatrix} 0 & -1 \\ 1 & 0 \end{bmatrix} \left(\begin{matrix} N_1 \\ -\frac{1}{\hat{\gamma}_1} \frac{\partial M_3}{\partial S} \end{matrix} \right) \right\} dS \quad . \quad (32)$$

The right-hand side of Eq. (27) becomes in components, using Eq. (10) for $\hat{\mathbf{n}}(S,t)$ and Eq. (29) for $\delta\psi(S,t)$:

$$RHS = \int_0^L \left\{ (\delta z_C(S,t))^T \left(R(\psi(S,t) \hat{n}(S,t) - \mathsf{m}_{\mathsf{A}(0)} \frac{\partial^2 z_C(S,t)}{\partial t^2} \right) \right\} dS$$

$$+\left[\left(\delta z_C\right)^T R(\psi(S,t)\,\hat{n}_E(S,t)+\left(\delta\frac{\partial z_C(S,t)}{\partial S}\right)^T\begin{bmatrix}-\sin\psi(S,t)\\ \cos\psi(S,t)\end{bmatrix}\frac{1}{\hat{\gamma}_1(S,t)}\hat{m}_E(S,t)\right]_{S=0}^{S=L} \quad (33)$$

Using Eqs. (32) and (33), the principle of virtual work, Eq. (27), gives

$$\int_0^L\left(\delta z_C\right)^T\left[R(\psi)\left\{\frac{\partial}{\partial S}\begin{pmatrix}N_1\\ -\frac{1}{\hat{\gamma}_1}\frac{\partial M_3}{\partial S}\end{pmatrix}+\frac{\partial\psi}{\partial S}\begin{bmatrix}0 & -1\\ 1 & 0\end{bmatrix}\begin{pmatrix}N_1\\ -\frac{1}{\hat{\gamma}_1}\frac{\partial M_3}{\partial S}\end{pmatrix}+\begin{pmatrix}\hat{n}_1\\ \hat{n}_2\end{pmatrix}\right\}-\mathsf{m}_{A(0)}\begin{pmatrix}\frac{\partial^2 z_{1C}}{\partial t^2}\\ \frac{\partial^2 z_{2C}}{\partial t^2}\end{pmatrix}\right]dS$$

$$+\left[\left(\delta z_C\right)^T R(\psi(S,t)\begin{pmatrix}\hat{n}_{1E}(S,t)-N_1(S,t)\\ \hat{n}_{2E}(S,t)+\frac{1}{\hat{\gamma}_1(S,t)}\frac{\partial M_3(S,t)}{\partial S}\end{pmatrix}\right]_{S=0}^{S=L}$$

$$+\left[\left(\delta\frac{\partial z_C(S,t)}{\partial S}\right)^T\begin{bmatrix}-\sin\psi(S,t)\\ \cos\psi(S,t)\end{bmatrix}\frac{1}{\hat{\gamma}_1(S,t)}\left\{\hat{m}_E(S,t)-M_3(S,t)\right\}\right]_{S=0}^{S=L}=0. \quad (34)$$

For arbitrary variations of $\delta z_{1C}(S,t)$ and $\delta z_{2C}(S,t)$, the first integral of Eq. (34) yields Eq. (21) as it should. The beam boundary conditions are:

(i) Either specify axial displacement or N_1

(ii) Either specify transverse displacement or $-\frac{1}{\hat{\gamma}_1}\frac{\partial M_3}{\partial S}(=N_2)$

(iii) Either specify the tangent of the curve of centroid or M_3

2.3.6 Development of C^1 Kirchhoff-Love Beam Elements

In finite element analyses, a curve of centroids is discretized by using two-node beam elements. To achieve a C^1-representation of the curve of centroids using for the Kirchhoff-Love beam elements, the continuity of the *z*-coordinates and their *S*-derivatives must be satisfied at each node, which joins two adjacent elements. A representative two-

node, Kirchhoff -Love beam element (e) with elemental node $\hat{1}$ and node $\hat{2}$, is shown in Fig. 2.5.

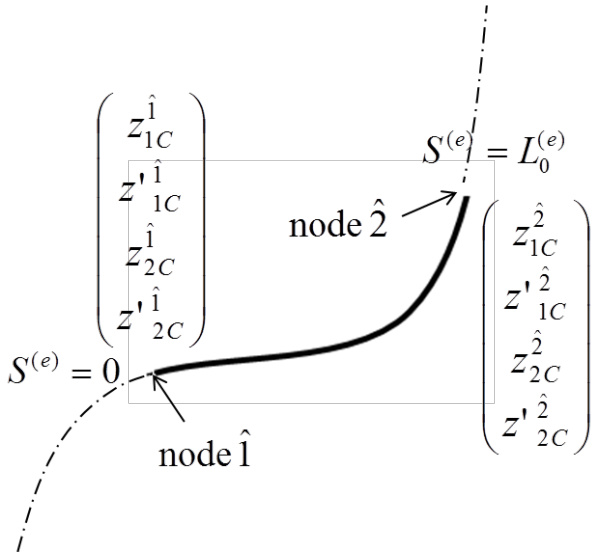

Figure 2.5: C^1 beam element

At time t=0, the reference curve of centroids is discretized into N_{el} elements, whereby the element number ranges from (e) =1 to N_{el}. In element (e), arc length increases from $S^{(e)}$=0 to the element length $L_0^{(e)}$, i.e., $0 \le S^{(e)} \le L_0^{(e)}$.

At time t, the same $S^{(e)}$ is used as an arc-parameter in element (e). To accomplish C^1 -connection of the discrete curve of centroids of adjacent elements, which meet at a shared node, four nodal displacements: $\left(z_{1C}^{\hat{j}} \quad z'_{1C}^{\hat{j}} \quad z_{2C}^{\hat{j}} \quad z'_{2C}^{\hat{j}}\right)^T$ for node $\hat{j} = \hat{1}$ and $\hat{2}$, where the prime denotes the S-derivative of the primed variable, for example, $z'_{1C}^{\hat{j}} \equiv \partial z_{1C}^{\hat{j}} / \partial S$ at node $\hat{j}$. In element (e) with the element length $L_0^{(e)}$at t=0, the z-coordinates of the position vector, $\mathbf{r}_C(S,t) = \mathbf{e}^I z_C(S,t)$ are interpolated by using the elemental nodal displacements $\left(\hat{d}^{(e)}(t)\right)$ and the matrix of shape functions $\left[\overline{\overline{N}}\right]$ as:

$$\underset{2\times1}{z_C^{(e)}}(S^{(e)},t) \equiv \begin{pmatrix} z_{1C}^{(e)} \\ z_{2C}^{(e)} \end{pmatrix}(S^{(e)},t) = \left[\underset{2\times8}{\overline{\overline{N}}}(S^{(e)},L_0^{(e)})\right]\left(\underset{8\times1}{\hat{d}^{(e)}}(t)\right). \tag{35}$$

The elemental nodal displacements $\left(\hat{d}^{(e)}(t)\right)$ are grouped for each z-component as:

$$\left(\underset{8\times1}{\hat{d}^{(e)}}(t)\right) = \begin{pmatrix} \underset{4\times1}{\hat{d}_1^{(e)}}(t) \\ \underset{4\times1}{\hat{d}_2^{(e)}}(t) \end{pmatrix}, \tag{36a}$$

$$\left(\underset{4\times1}{\hat{d}_1^{(e)}}(t)\right) \equiv \begin{pmatrix} \hat{z_{1C}^{1}}(t) \\ \hat{z'_{1C}^{1}}(t) \\ \hat{z_{1C}^{2}}(t) \\ \hat{z'_{1C}^{2}}(t) \end{pmatrix}, \tag{36b}$$

$$\left(\underset{4\times1}{\hat{d}_2^{(e)}}(t)\right) \equiv \begin{pmatrix} \hat{z_{2C}^{1}}(t) \\ \hat{z'_{2C}^{1}}(t) \\ \hat{z_{2C}^{2}}(t) \\ \hat{z'_{2C}^{2}}(t) \end{pmatrix}, \tag{36c}$$

The matrix of shape functions $\left[\overline{\overline{N}}\right]$ is defined as:

$$\left[\underset{2\times8}{\overline{\overline{N}}}(S^{(e)},L_0^{(e)})\right] \equiv \begin{bmatrix} \underset{1\times4}{\widetilde{N}}(S^{(e)},L_0^{(e)}) & \underset{1\times4}{0} \\ \underset{1\times4}{0} & \underset{1\times4}{\widetilde{N}}(S^{(e)},L_0^{(e)}) \end{bmatrix}, \tag{37a}$$

where

$$\underset{1\times4}{\widetilde{N}}(S^{(e)},L_0^{(e)}) \equiv \left[\widetilde{N}_1(S^{(e)},L_0^{(e)}) \quad \widetilde{N}_2(S^{(e)},L_0^{(e)}) \quad \widetilde{N}_3(S^{(e)},L_0^{(e)}) \quad \widetilde{N}_4(S^{(e)},L_0^{(e)})\right], \tag{37b}$$

and the four shape functions, which enable C^1-interpolation of the curve of centroids are defined as:

$$\widetilde{N}_1(S^{(e)}, L_0^{(e)}) = 1 - 3\left(\frac{S^{(e)}}{L_0^{(e)}}\right)^2 + 2\left(\frac{S^{(e)}}{L_0^{(e)}}\right)^3, \tag{38a}$$

$$\widetilde{N}_2(S^{(e)}, L_0^{(e)}) = S^{(e)}\left\{\left(\frac{S^{(e)}}{L_0^{(e)}}\right) - 1\right\}^2, \tag{38b}$$

$$\widetilde{N}_3(S^{(e)}, L_0^{(e)}) = \left(\frac{S^{(e)}}{L_0^{(e)}}\right)^2 \left\{3 - 2\left(\frac{S^{(e)}}{L_0^{(e)}}\right)\right\}, \tag{38c}$$

$$\widetilde{N}_4(S^{(e)}, L_0^{(e)}) = \frac{\left(S^{(e)}\right)^2}{L_0^{(e)}}\left\{\left(\frac{S^{(e)}}{L_0^{(e)}}\right) - 1\right\}. \tag{38d}$$

They are plotted in Fig. 2.6.

The C^1-cubic shape functions, $\widetilde{N}(S^{(e)}, L_0^{(e)})$, have been used for the interpolation of transverse displacement in linear Euler-Bernoulli beam elements [16]. In the curved Kirchhoff-Love beam elements, the C^1-shape functions are utilized for both z_{1C}-interpolation and z_{2C}-interpolation of the element curve of centroids, as shown in Eq. (35).

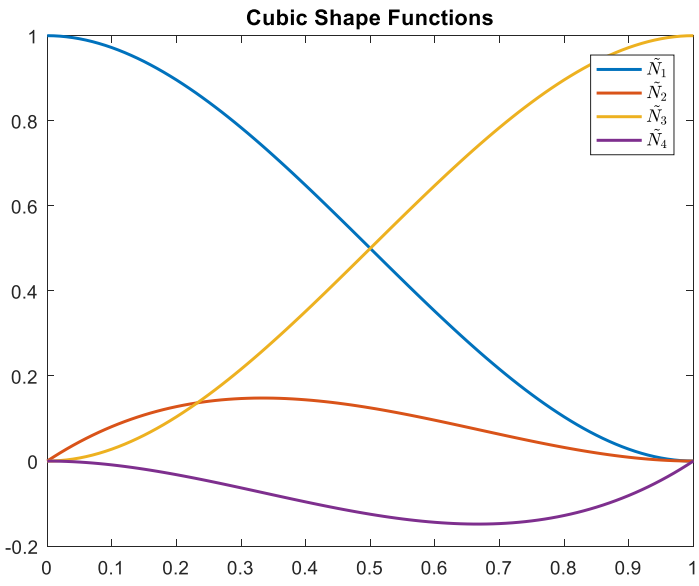

Figure 2.6: C^1 -cubic shape functions used for the Kirchhoff-Love beam elements

Using the coordinates of the curve of centroids, in element (e), their S-derivatives are also expressed by the nodal coordinates as:

$$\frac{\partial z_C^{(e)}(S^{(e)},t)}{\partial S} \equiv \underset{2\times 8}{\left[\overline{\overline{N}}'(S^{(e)},L_0^{(e)})\right]} \underset{8\times 1}{\left(\hat{d}^{(e)}(t)\right)}, \tag{39a}$$

where $\left[\overline{\overline{N}}'\right]$ denotes the S-derivative of the matrix of shape functions as:

$$\underset{2\times 8}{\left[\overline{\overline{N}}'(S^{(e)},L_0^{(e)})\right]} \equiv \begin{bmatrix} \underset{1\times 4}{\partial\tilde{N}(S^{(e)},L_0^{(e)})/\partial S} & \underset{1\times 4}{0} \\ \underset{1\times 4}{0} & \underset{1\times 4}{\partial\tilde{N}(S^{(e)},L_0^{(e)})/\partial S} \end{bmatrix}. \tag{39b}$$

Similarly, the second derivative of the curve of centroids are expressed by the nodal coordinates as:

$$\frac{\partial^2 z_C^{(e)}(S^{(e)},t)}{\partial S^2} \equiv \underset{2\times 8}{\left[\overline{\overline{N}}''(S^{(e)},L_0^{(e)})\right]} \underset{8\times 1}{\left(\hat{d}^{(e)}(t)\right)}, \tag{40a}$$

where $\left[\underset{}{\overset{=}{N}}''\right]$ denotes the second *S*-derivative of the matrix of shape functions as:

$$\underset{2\times 8}{\left[\overset{=}{N}''(S^{(e)},L_0^{(e)})\right]} \equiv \begin{bmatrix} \underset{1\times 4}{\partial^2\widetilde{N}(S^{(e)},L_0^{(e)})/\partial S^2} & \underset{1\times 4}{0} \\ \underset{1\times 4}{0} & \underset{1\times 4}{\partial^2\widetilde{N}(S^{(e)},L_0^{(e)})/\partial S^2} \end{bmatrix}. \tag{40b}$$

In FE codes, elemental integrations are performed by using the Gauss quadrature. Therefore, beam strain variables and beam stress variables are all evaluated at the integration points, not at every point on the curve of centroids [10, 16]. In the Kirchhoff-Love beam elements, four-point Gauss quadrature is utilized.

At each integration point in element (e), $z_C(S^{(e)},t)$, $\partial z_C(S^{(e)},t)/\partial S$, and $\partial^2 z_C(S^{(e)},t)/\partial S^2$, are now expressed by the matrix of shape functions $\left[\overline{\overline{N}}\right]$, its *S*-derivatives, and elemental nodal displacements, $\left(\hat{d}^{(e)}(t)\right)$. More specifically, Eq. (39a) enables the evaluation of the beam strain variables, $\hat{\gamma}_1(S,t)$ in Eq. (20a), as well as $\cos\psi(S,t)$ and $\sin\psi(S,t)$ in Eq. (20b), using the nodal displacements.

$$\hat{\gamma}_1(S^{(e)},t) = \sqrt{\left(\hat{d}^{(e)}(t)\right)^T \left[\underset{}{\overset{=}{N}}'(S^{(e)},L_0^{(e)})\right]^T \left[\underset{}{\overset{=}{N}}'(S^{(e)},L_0^{(e)})\right]\left(\hat{d}^{(e)}(t)\right)}. \tag{41}$$

$$\begin{pmatrix} \cos\psi(S^{(e)},t) \\ \sin\psi(S^{(e)},t) \end{pmatrix} = \frac{1}{\hat{\gamma}_1(S^{(e)},t)} \underset{2\times 8}{\left[\overset{=}{N}'(S^{(e)},L_0^{(e)})\right]} \underset{8\times 1}{\left(\hat{d}^{(e)}(t)\right)}. \tag{42}$$

Next, Eq. (38a) facilitates the computations of $\partial\psi(S,t)/\partial S$ in Eq. (23a) and $\partial\psi(S,0)/\partial S$ in Eq. (24) using the nodal displacements $\left(\hat{d}^{(e)}(t)\right)$ and $\left(\hat{d}^{(e)}(0)\right)$, respectively.

$$\frac{\partial \psi(S^{(e)},t)}{\partial S} = \frac{1}{\hat{\gamma}_1(S^{(e)},t)}\left[-\sin\psi(S^{(e)},t) \quad \cos\psi(S^{(e)},t)\right]\left[\overline{\overline{N}}''(S^{(e)},L_0^{(e)})\right]\left(\hat{d}^{(e)}(t)\right), \tag{43a}$$

$$\frac{\partial \psi(S^{(e)},0)}{\partial S} = \left[-\sin\psi(S^{(e)},0) \quad \cos\psi(S^{(e)},0)\right]\left[\overline{\overline{N}}''(S^{(e)},L_0^{(e)})\right]\left(\hat{d}^{(e)}(0)\right). \tag{43b}$$

At each integration point of element (e), beam axial force $N_1(S^{(e)},t)$ is computed using Eq. (16a) with Eq. (41) as:

$$N_1^{(e)}(S^{(e)},t) = EA\left\{\sqrt{\left(\hat{d}^{(e)}(t)\right)^T\left[\overline{\overline{N}}'(S^{(e)},L_0^{(e)})\right]^T\left[\overline{\overline{N}}'(S^{(e)},L_0^{(e)})\right]\left(\hat{d}^{(e)}(t)\right)}-1\right\}. \tag{44}$$

The beam moment $M_3(S^{(e)},t)$ is evaluated using Eq. (26) with Eqs. (43a, b) as:

$$M_3^{(e)}(S^{(e)},t) = EI_3\frac{1}{\hat{\gamma}_1(S^{(e)},t)}\left[-\sin\psi(S^{(e)},t) \quad \cos\psi(S^{(e)},t)\right]\left[\overline{\overline{N}}''(S^{(e)},L_0^{(e)})\right]\left(\hat{d}^{(e)}(t)\right)$$

$$-EI_3\left[-\sin\psi(S^{(e)},0) \quad \cos\psi(S^{(e)},0)\right]\left[\overline{\overline{N}}''(S^{(e)},L_0^{(e)})\right]\left(\hat{d}^{(e)}(0)\right). \tag{45}$$

The virtual displacements, $\delta z_C(S,t)$, of the curve of centroids is also interpolated using virtual nodal displacements $\delta\hat{d}_1^{(e)}(t)$ and $\delta\hat{d}_2^{(e)}(t)$ in element (e) as:

$$\delta z_C^{(e)}(S^{(e)},t) \equiv \begin{pmatrix}\delta z_{1C}^{(e)}\\ \delta z_{2C}^{(e)}\end{pmatrix}(S^{(e)},t) = \underset{1\times 4}{\left[\overline{\overline{N}}(S^{(e)},L_0^{(e)})\right]}\underset{8\times 1}{\begin{pmatrix}\delta\hat{d}^{(e)}(t)\end{pmatrix}}, \tag{46a}$$

where elemental virtual displacements are

$$\underset{8\times 1}{\left(\delta\hat{d}^{(e)}(t)\right)} \equiv \begin{pmatrix}\underset{4\times 1}{\delta\hat{d}_1^{(e)}(t)}\\ \underset{4\times 1}{\delta\hat{d}_2^{(e)}(t)}\end{pmatrix}. \tag{46b}$$

Similarly, the *S*-derivatives of virtual displacements δz_C are expressed in element (*e*) in terms of the *S*-derivatives of shape functions, defined in Eqs. (39b) and (40b), and virtual nodal displacements:

$$\frac{\partial \delta z_C^{(e)}}{\partial S}(S^{(e)},t) \equiv \begin{pmatrix} \dfrac{\partial \delta z_{1C}^{(e)}}{\partial S} \\ \dfrac{\partial \delta z_{2C}^{(e)}}{\partial S} \end{pmatrix}(S^{(e)},t) = \left[\underset{1\times 4}{\overline{\overline{N}}'(S^{(e)},L_0^{(e)})}\right]\left(\underset{8\times 1}{\delta \hat{d}^{(e)}(t)}\right), \tag{47}$$

$$\frac{\partial^2 \delta z_C^{(e)}}{\partial S^2}(S^{(e)},t) \equiv \begin{pmatrix} \dfrac{\partial^2 \delta z_{1C}^{(e)}}{\partial S^2} \\ \dfrac{\partial^2 \delta z_{2C}^{(e)}}{\partial S^2} \end{pmatrix}(S^{(e)},t) = \left[\underset{1\times 4}{\overline{\overline{N}}''(S^{(e)},L_0^{(e)})}\right]\left(\underset{8\times 1}{\delta \hat{d}^{(e)}(t)}\right). \tag{48}$$

Now, in a generic element (*e*), all the functions of the virtual displacements and their S-derivatives are expressed by nodal virtual displacements in Eq. (43b). Next, the virtual strain variables, which appear in the principle of virtual work, Eq. (27), are expressed using the nodal virtual displacements.

The virtual axial strain $\delta \hat{\gamma}_1(S^{(e)},t)$ at a Gauss integration point in element (*e*) is expressed in terms of the virtual nodal displacements by substituting Eq. (39a) into Eq. (28a) as:

$$\delta \hat{\gamma}_1(S^{(e)},t) = \left[\cos\psi(S^{(e)},t) \quad \sin\psi(S^{(e)},t)\right]\left[\overline{\overline{N}}'(S^{(e)},L_0^{(e)})\right]\left(\delta \hat{d}^{(e)}(t)\right). \tag{49}$$

Equation (49) is also obtained by taking the variation of Eq. (41) and using Eq. (42), as it should.

The virtual curvature in Eq. (30a) is expressed by nodal virtual displacements using both Eqs. (47) and (48) as:

$$\frac{\partial \delta\psi(S^{(e)},t)}{\partial S} = \left\{\frac{1}{\hat{\gamma}_1(S^{(e)},t)}\left[-\sin\psi(S^{(e)},t) \quad \cos\psi(S^{(e)},t)\right]\right\}\left[\overline{\overline{N}}''(S^{(e)},L_0^{(e)})\right]\left(\delta\hat{d}^{(e)}(t)\right)$$

$$+\frac{\partial}{\partial S^{(e)}}\left\{\frac{1}{\hat{\gamma}_1(S^{(e)},t)}\left[-\sin\psi(S^{(e)},t) \quad \cos\psi(S^{(e)},t)\right]\right\}\left[\overline{\overline{N}}'(S^{(e)},L_0^{(e)}\right]\left(\delta\hat{d}^{(e)}(t)\right), \quad (50a)$$

The *S*-derivative in the second term on the right-hand side is evaluated using Eqs. (23) and (4a) together with Eq. (40a) as follows:

$$\frac{\partial \delta\psi(S^{(e)},t)}{\partial S} = \left\{\frac{1}{\hat{\gamma}_1(S^{(e)},t)}\left[-\sin\psi(S^{(e)},t) \quad \cos\psi(S^{(e)},t)\right]\right\}\left[\overline{\overline{N}}''(S^{(e)},L_0^{(e)})\right]\left(\delta\hat{d}^{(e)}(t)\right)$$

$$-\left(\hat{d}^{(e)}(t)\right)^T\left[\overline{\overline{N}}''(S^{(e)},L_0^{(e)})\right]^T\left(\frac{1}{\hat{\gamma}_1(S^{(e)},t)}\right)^2\begin{bmatrix}-\sin 2\psi & \cos 2\psi\\ \cos 2\psi & \sin 2\psi\end{bmatrix}\left[\overline{\overline{N}}'(S^{(e)},L_0^{(e)}\right]\left(\delta\hat{d}^{(e)}(t)\right), \quad (50b)$$

where

$$\begin{pmatrix}\cos 2\psi\\ \sin 2\psi\end{pmatrix} = \begin{pmatrix}\cos^2\psi(S^{(e)},t)-\sin^2\psi(S^{(e)},t)\\ 2\cos\psi(S^{(e)},t)\sin\psi(S^{(e)},t)\end{pmatrix}. \quad (50c)$$

It is easily checked that Eq. (48b) is also obtained by taking the variation of Eq. (23a) using Eqs. (28a) and (29) with Eq. (47).

2.3.7 Nonlinear FE Equations of Motion

The global (arbitrary) virtual-displacements $(\delta d(t))$are assembled from elemental virtual displacements $\left(\delta\hat{d}^{(e)}(t)\right)$ utilizing the element connectivity input data and excluding vanishing virtual displacements since virtual nodal displacements vanish when

their nodal values are prescribed. Corresponding to $(\delta d(t))$, the global, unknown nodal-displacements are defined as $(d(t))$ from $\left(\hat{d}^{(e)}(t)\right)$, see for example, [10, 16].

The virtual work equation, Eq. (27) is reordered, and integration over the entire curve of centroids is performed on each element using the Gauss quadrature as:

$$\sum_{e=1}^{Nel}\int_{S=0}^{L_0^{(e)}}\left(\delta z_C(S,t)\right)^T\cdot\left(\mathsf{m}_{A(0)}\frac{\partial^2 z_C(S,t)}{\partial t^2}\right)dS+\sum_{e=1}^{Nel}\int_{S=0}^{L_0^{(e)}}\begin{pmatrix}\delta\hat{\gamma}_1\\ \partial\delta\psi/\partial S\end{pmatrix}^T\begin{pmatrix}N_1(S,t)\\ M_3(S,t)\end{pmatrix}dS$$

$$-\sum_{e=1}^{Nel}\int_{S=0}^{L_0^{(e)}}\left(\delta z_C(S,t)\right)^T R(\psi(S,t))\,\hat{n}(S,t)\,dS-\left(\delta d(t)\right)^T\left(F_E(t)\right)=0, \qquad (51a)$$

where $(F_E(t))$, acting on $(\delta d(t))$, is the nodal forces, which express the virtual work in Eq. (26) induced by the boundary forces and couple, such that

$$\left(\delta d(t)\right)^T\left(F_E(t)\right)=\left[\left(\delta z_C(S,t)\right)^T R(\psi(S,t)\hat{n}_E(S,t)+\delta\psi(S,t)\hat{m}_E(S,t)\right|_{S=0}^{S=L}. \qquad (51b)$$

2.3.8 Element Mass Matrix

The first integral in Eq. (51a) represents the negative of the virtual work by inertial forces and defines element mass matrices. The acceleration in element (e) is expressed from Eq. (35) by the nodal acceleration as:

$$\underset{2\times1}{\frac{\partial^2}{\partial t^2}z_C^{(e)}}(S^{(e)},t)\equiv\left[\underset{2\times8}{\overline{\overline{N}}(S^{(e)},L_0^{(e)})}\right]\frac{d^2}{dt^2}\left(\underset{8\times1}{\hat{d}^{(e)}(t)}\right). \qquad (52)$$

The first integral is written using Eqs. (44a) and (52) as

$$\int_{S=0}^{L_0^{(e)}}\left(\delta z_C(S,t)\right)^T\cdot\left(\mathsf{m}_{A(0)}\frac{\partial^2 z_C(S,t)}{\partial t^2}\right)dS=\left(\delta\hat{d}^{(e)}(t)\right)^T\left[M^{(e)}\right]\frac{d^2}{dt^2}\left(\hat{d}^{(e)}(t)\right), \qquad (53a)$$

where the element mass matrix $\lfloor M^{(e)} \rfloor$ is a constant matrix, reflecting the conservation of mass:

$$\left[\underset{8\times 8}{M^{(e)}} \right] \equiv \int_{S^{(e)}=0}^{L_0^{(e)}} \left[\overline{\overline{N}}(S^{(e)}, L_0^{(e)}) \right]^T \mathsf{m}_{A(0)} \left[\overline{\overline{N}}(S^{(e)}, L_0^{(e)}) \right] dS^{(e)}$$

$$= \begin{bmatrix} \underset{4\times 4}{M_{11}^{(e)}} & \underset{4\times 4}{0} \\ \underset{4\times 4}{0} & \underset{4\times 4}{M_{11}^{(e)}} \end{bmatrix}, \tag{53b}$$

where

$$\left[\underset{4\times 4}{M_{11}^{(e)}} \right] = \mathsf{m}_{A(0)} L_0^{(e)} \begin{bmatrix} \frac{13}{35} & \frac{11L_0^{(e)}}{210} & \frac{9}{70} & -\frac{13L_0^{(e)}}{420} \\ \frac{11L_0^{(e)}}{210} & \frac{(L_0^{(e)})^2}{105} & \frac{13L_0^{(e)}}{420} & -\frac{(L_0^{(e)})^2}{140} \\ \frac{9}{70} & \frac{13L_0^{(e)}}{420} & \frac{13}{35} & -\frac{11L_0^{(e)}}{210} \\ -\frac{13L_0^{(e)}}{420} & -\frac{(L_0^{(e)})^2}{140} & -\frac{11L_0^{(e)}}{210} & \frac{(L_0^{(e)})^2}{105} \end{bmatrix}. \tag{53c}$$

2.3.9 Element Internal Force Vector

The second integral in Eq. (51a) represents the virtual strain energy and defines internal force vector $(\hat{P}^{(e)}(t))$ when it is evaluated on element (e) as:

$$\int_{S=0}^{L_0^{(e)}} \begin{pmatrix} \delta\hat{\gamma}_1 \\ \dfrac{\partial\delta\psi}{\partial S} \end{pmatrix}^T \begin{pmatrix} N_1(S,t) \\ M_3(S,t) \end{pmatrix} dS = \left(\delta\hat{d}^{(e)}(t) \right)^T \left(\hat{P}^{(e)}(t) \right), \tag{54}$$

The above integration is performed by using the Gauss quadrature. To compute the internal force vector, the virtual beam strains are expressed by virtual nodal displacements through $[B^{(e)}]$-matrix at each integration point:

$$\begin{pmatrix} \delta\hat{\gamma}_1 \\ \dfrac{\partial\delta\psi}{\partial S} \end{pmatrix}(S^{(e)},t) = \left[B^{(e)}(t)\right]\left(\delta\hat{d}^{(e)}(t)\right), \tag{55a}$$

where $[B^{(e)}(t)]$ is defined from Eqs. (47) and (48b) as

$$\underset{2\times 8}{\left[B^{(e)}(t)\right]} = \begin{bmatrix} \underset{1\times 8}{B_1^{(e)}(t)} \\ \underset{1\times 8}{B_2^{(e)}(t)} \end{bmatrix}, \tag{55b}$$

in which the submatrices are all functions of current nodal displacements:

$$\underset{1\times 8}{\left[B_1^{(e)}(t)\right]} = \left[\cos\psi(S^{(e)},t) \quad \sin\psi(S^{(e)},t)\right]\underset{2\times 8}{\left[\overline{\overline{N}}'(S^{(e)},L_0^{(e)})\right]}, \tag{55c}$$

$$\underset{1\times 8}{\left[B_2^{(e)}(t)\right]} = \left\{\frac{1}{\hat{\gamma}_1(S^{(e)},t)}\left[-\sin\psi(S^{(e)},t) \quad \cos\psi(S^{(e)},t)\right]\right\}\left[\overline{\overline{N}}''(S^{(e)},L_0^{(e)})\right]$$

$$-\left(\hat{d}^{(e)}(t)\right)^T\left[\overline{\overline{N}}''(S^{(e)},L_0^{(e)})\right]^T\left(\frac{1}{\hat{\gamma}_1(S^{(e)},t)}\right)^2\begin{bmatrix} -\sin 2\psi & \cos 2\psi \\ \cos 2\psi & \sin 2\psi \end{bmatrix}\left[\overline{\overline{N}}'(S^{(e)},L_0^{(e)})\right]. \tag{55d}$$

As a result, the internal force vector is defined by substituting Eqs. (55a), (44), and (45) into Eq. (54):

$$\left(\hat{P}^{(e)}(t)\right) = \int_{S=0}^{L_0^{(e)}}\left[B^{(e)}(t)\right]^T\begin{pmatrix} N_1(S,t) \\ M_3(S,t) \end{pmatrix}dS. \tag{56}$$

2.3.10 Element External Force Vector due to Distributed Loads

The third integral of Eq. (51a) represents the virtual work by the distributed load $\hat{n}(S,t)$ decomposed with respect to the moving frame. This integral defines the effective

nodal force due to the distributed load, where $\hat{n}(S,t)$ is prescribed at the integration points of element (e).

$$\int_{S=0}^{L_0^{(e)}} \left(\delta z_C(S,t)\right)^T R(\psi(S,t))\ \hat{n}(S,t)\, dS = \left(\delta \hat{d}^{(e)}(t)\right)^T \left(\hat{F}_B^{(e)}(t)\right). \tag{57}$$

The substitution of Eq. (46a) into the above with the components of the rotation matrix evaluated using Eq. (42) defines the effective nodal force vector:

$$\left(\hat{F}_B^{(e)}(t)\right) = \int_{S=0}^{L_0^{(e)}} \left[\overline{\overline{N}}(S^{(e)}, L_0^{(e)})\right]^T R(\psi(S,t))\ \hat{n}(S,t)\, dS\ . \tag{58}$$

Equation (51a) is now written as

$$\sum_{e=1}^{Nel} \left(\delta \hat{d}^{(e)}(t)\right)^T \left\{ \left[M^{(e)}\right] \frac{d^2}{dt^2} \left(\hat{d}^{(e)}(t)\right) + \left(\hat{P}^{(e)}(t)\right) - \left(\hat{F}_B^{(e)}(t)\right) \right\} - \left(\delta d(t)\right)^T \left(F_E(t)\right) = 0\ . \tag{59}$$

When Eq. (59) is assembled for global degrees of freedom, a system of nonlinear FE equations of motion is finally obtained:

$$\left(\delta d(t)\right)^T \left\{ \left[M\right] \left(\ddot{d}(t)\right) + \left(P(t)\right) - \left(F_B(t)\right) - \left(F_E(t)\right) \right\} = 0\ , \tag{60}$$

where $[M]$ denotes the global mass matrix, $(P(t))$ expressed the internal force, $(F_B(t))$ represents the nodal force due to the distributed loads $\hat{n}(S,t)$, and $(F_E(t))$ is the nodal force by the boundary forces and couples, defined in Eq. (51b).

The FE equations of motion at time t becomes

$$\left[M\right] \left(\ddot{d}(t)\right) + \left(P(t)\right) - \left(F_B(t)\right) - \left(F_E(t)\right) = \left(0\right). \tag{61}$$

For the time integration, the Newmark method is employed, and at each time step, the Newton method is utilized to iterate to reduce residual forces. Both the Newmark time

integration method and the Newton method to solve time-dependent nonlinear FE equations are expertly presented by Belytschko, Liu, and Moran [11]. Therefore, the solution process of Eq. (61) is not shown in the report.

2.4 Preliminary Experiments

Preliminary experiments were conducted to test and compare the ribbed caudal fin with the results of the FE code, which will be published at a later time.

2.4.1 Experimental Setup

To observe the effects of webs in a caudal fin, a rig was designed and implemented to generate consistent deformation of a flexible acrylic caudal fin at varying frequencies. On the caudal fin, notches are placed to add and remove webs at different locations along the length of the fin. Attached at the front-end of the base is a servomotor that actuates the caudal fin, and a second rotation point gives more structural support across the rest of said fin. Also, the attachments offer a separation between the fin segments, which can be seen in Fig. 2.7.

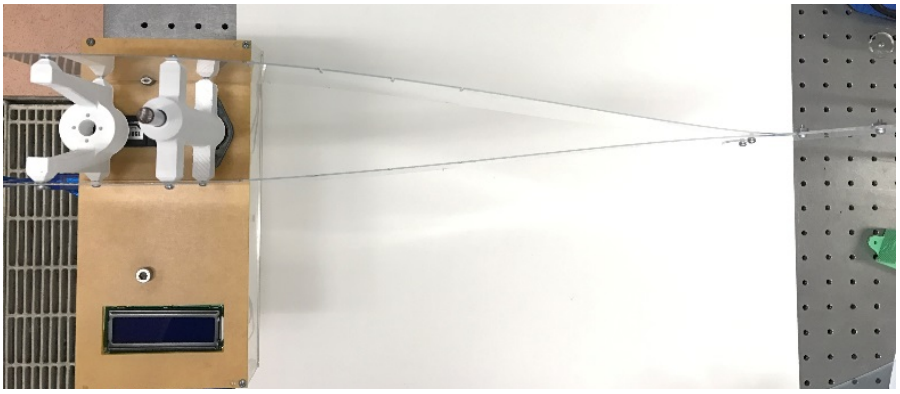

Figure 2.7: Separation of flexible caudal fin segments

The complete device is shown in Fig. 2.8, which includes the acrylic caudal fin connected to the actuation device driven by an Arduino microcontroller. It is important to note that the portion of the caudal fin after the rotational attachments (in white) is only considered in the experiments. To measure the amplitudes, a camera recorded multiple experiments with differing rotational speeds. Afterwards, the video was analyzed using MATLAB.

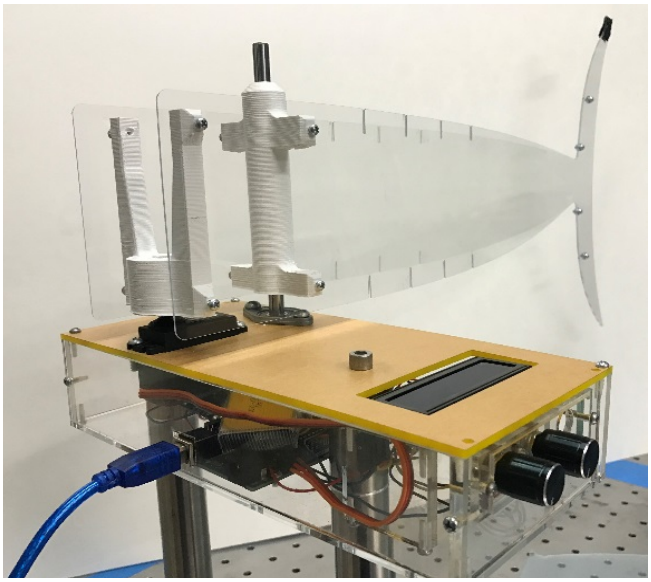

Figure 2.8: Caudal fin testing device

2.4.2 Experimental Results

Several preliminary tests at a fixed frequency were conducted to observe the behavior of the caudal fin with zero and one web. For each test, the radius of curvature at the frame of maximum amplitude was computed for highlighted points. The displacement data was recorded at various frames in the footage, fitted to a quadratic polynomial, and was then used to calculate the radius of curvature using the expression below:

$$\kappa = \frac{\left(1+\left(\frac{dy}{dx}\right)^2\right)^{\frac{3}{2}}}{\left|\frac{d^2y}{dx^2}\right|} \tag{61}$$

The first test conducted was for a ribbed caudal fin with zero added webs at a 1.7167 Hz frequency. As can be shown from Fig. 2.9, the oscillatory motion caused a large tail displacement of $\approx 10''$, or 63% of the length, not including the white structural elements.

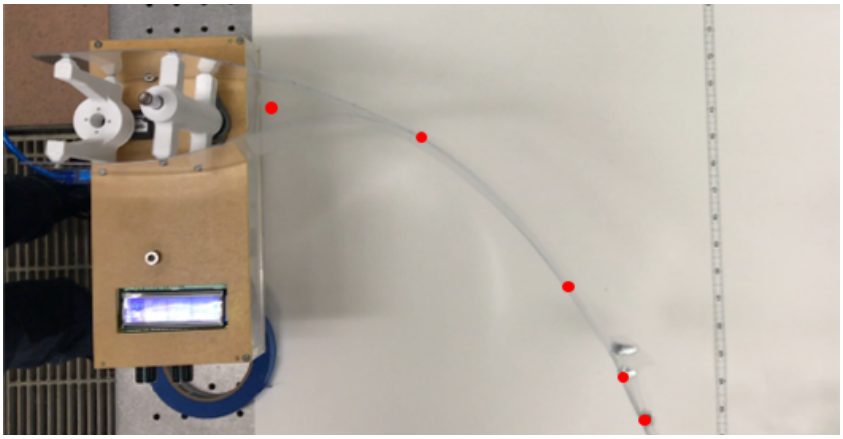

Figure 2.9: Zero web testing of the actuated caudal fin showing maximum displacement and points (red) for curvature calculation

By analyzing the displacement at several points across the beam, the radius of curvature can be calculated at the red points after the fitting the points to a quadratic polynomial. The quadratic polynomial used: $-0.6287x^2 + 0.122x + 0.0104$, results in the following radius of curvature values for the points shown above: κ =0.4157,1.892,11.8666,23.4826 and 33.7692 respectively.

The second set of experiments conducted included a ribbed caudal fin with a single web. As shown below in Fig. 2.10, the maximum displacement with a single web was $\approx 4''$ or approximately 25% of the length. The web caused a decrease in amplitude of $\approx 6''$ or 60% of the maximum displacement measured without a rib. The calculated radii

of curvature for the shown red points below were as follows: $\kappa = 3.7874, 4.1584, 4.7484, 4.9916$, and 5.1413 using the following quadratic polynomial fit: $-0.07x^2 - 0.1406x - 0.0223$.

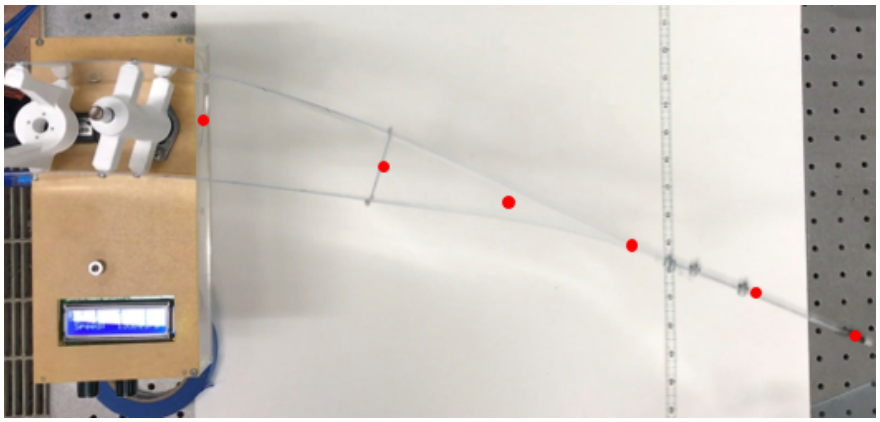

Figure 2.10: Single web testing of the actuated caudal fin showing maximum displacement and points (red) for curvature calculation

The addition of the web was shown to cause much higher stability, especially at higher frequencies of oscillation. Also, various tests featuring additional ribs closer to the actuation point had the same amount of deflection as the farthest back rib.

2.5 Appendix

For linear beams, it is possible to obtain analytical solutions. Such solutions may be used to validate nonlinear FE codes for small deformation at some equilibrium configuration. Furthermore, the analytical solutions give guidelines for time increment or load increment as well as the contributions of transverse shear deformation.

2.5.1 Equations of Motion for Small Deformation of Initially Straight Beams

For initially straight beams in the z_1-direction, parameterized by its coordinate S, the deformed configuration, Eq. (1) may be expressed by using displacement components $u_1(S,t)$ in the z_1-direction and $u_2(S,t)$ in the z_2-direction as

$$\mathbf{r}_C(S,t) = \begin{pmatrix} \mathbf{e}_1^I & \mathbf{e}_2^I \end{pmatrix} \begin{pmatrix} S + u_1(S,t) \\ u_2(S,t) \end{pmatrix}. \tag{A.1}$$

The transverse shear strain $\hat{\gamma}_2(S,t)$ is the reduction of the angle between the principal axis $\mathbf{e}_2(S,t)$ and the tangent vector, $\hat{\boldsymbol{\gamma}}(S,t)$, from $\pi/2$ radian. Observing that the angle of $\hat{\boldsymbol{\gamma}}(S,t)$ from $\mathbf{e}_1^I$ is expressed by $\partial u_2/\partial S$, while the angle of $\mathbf{e}_1(S,t)$ from $\mathbf{e}_1^I$ is $\psi(S,t)$, the reduction of the angle between $\mathbf{e}_2(S,t)$ and $\hat{\boldsymbol{\gamma}}(S,t)$ from $\pi/2$ is written as:

$$\hat{\gamma}_2 \equiv \frac{\partial u_2}{\partial S} - \psi. \tag{A.2}$$

In the *Timoshenko beam* model, transverse shear deformation is included, $\hat{\gamma}_2 \neq 0$, the deformed configuration of Timoshenko beams are expressed by $\{u_1(S,t) \quad u_2(S,t) \quad \psi(S,t)\}$ including $\psi(S,t)$. For small deformation of straight beams adopting the normality of rigid cross sections during deformation is known as the "Euler-Bernoulli beam model". In the Euler-Bernoulli beam, $\psi(S,t)$ is expressed by the S-derivative of the transverse displacement:

$$\psi(S,t) = \tan^{-1}\left(\frac{\dfrac{\partial u_2}{\partial S}}{1 + \dfrac{\partial u_1}{\partial S}} \right) \approx \frac{\partial u_2}{\partial S} \tag{A.3}$$

As a result, the deformation of the *Euler-Bernoulli beam* is described by using just axial displacement $u_1(S,t)$ and transverse displacement $u_2(S,t)$, without $\psi(S,t)$.

By linearizing Reissner's curved beam equations, in what follows, the Timoshenko beam equations are first derived. Subsequently, by incorporating the assumption of negligible transverse shear deformation, the Euler-Bernoulli beam equations are derived.

2.5.2 Timoshenko Beam Equations

Using Eq. (A.1) for straight beams, the linearization of Eq. (15) for small deformation yields:

$$\frac{\partial}{\partial S} N_1(S,t) + \hat{n}_1(S,t) = \mathsf{m}_{\mathsf{A}(0)} \frac{\partial^2 u_1(S,t)}{\partial t^2}, \tag{A.4a}$$

$$\frac{\partial}{\partial S} N_2(S,t) + \hat{n}_2(S,t) = \mathsf{m}_{\mathsf{A}(0)} \frac{\partial^2 u_2(S,t)}{\partial t^2}, \tag{A.4b}$$

Linearization of Eq. (13) further incorporates the assumption: $\hat{\gamma}_1 \approx 1$.

$$\frac{\partial}{\partial S} M_3(S,t) + N_2(S,t) + \hat{m}_3(S,t) = J_{3C(0)} \frac{\partial^2}{\partial t^2} \psi(S,t). \tag{A.5}$$

For elastic beams, Hooke's law relates the beam axial force, shear force, and bending moment (per unit reference line of centroids) to axial strain, $\partial u_1 / \partial S$, shear strain, $\hat{\gamma}_2 = \partial u_2 / \partial S - \psi$ from Eq. (9b), and curvature, $\partial \psi / \partial S$. For a homogeneous beam with Young's modulus E, shear modulus G, area of cross section A, and areal moment of inertia I_3, Hooke's law yields

$$N_1(S,t) = EA \frac{\partial}{\partial S} u_1(S,t), \tag{A.6a}$$

$$N_2(S,t) = GA_s \left(\frac{\partial}{\partial S} u_2(S,t) - \psi(S,t) \right), \tag{A.6b}$$

$$M_3(S,t) = E I_3 \frac{\partial}{\partial S}\psi(S,t), \tag{A.7}$$

where A_s is the area of cross section for shear deformation (to incorporate the shear correction factor).

For static problems, the Timoshenko beam equations can be solved analytically and results can be compared to those of the Euler-Bernoulli beam equations, which neglects the effect of transverse shear deformation. The analytical solution of Timoshenko beams under uniform distributed loads was available for both cantilever beams and simply supported beams [8, 9].

In the small deformation analyses, the axial and transverse deformations are decoupled. The axial deformation of the beam or rod is governed by Eqs.(A.4a) and (A.6a), while the transverse deformation of the beam is solved by using Eq. (A.4b) and (A.5) with Eqs. (A.6b) and (A.7). (For small deformation of beams, the coupling of the transverse and axial deformation of beams was first included for linear plate analyses by von Karman, see for example, Fung [14].)

Next, the Euler-Bernoulli beam equations are derived by neglecting the transverse shear stain.

2.5.3 The Euler Bernoulli Beam Equations

In the beam model, the transverse shear strain $\hat{\gamma}_2 = \partial u_2 / \partial S - \psi$ is neglected:

$$\psi(S,t) = \frac{\partial u_2(S,t)}{\partial S}. \tag{A.8}$$

The constraint of zero transverse shear strain in Eq. (A.8) makes the shear force constitutive equation, Eq. (A.6b) invalid. Since nonzero shear force always exists in deforming beams, Eq. (A.6b) only makes sense at simultaneous limits of $GA_s \to \infty$ and $\hat{\gamma}_2 \to 0$. This indicates that shear force become a *reactive force*, for which the shear constitutive relation, Eq. (A.6b), does not hold, (but equilibrium equations hold).

For thin beams, both transverse shear strain, $\hat{\gamma}_2$, and the mass moment of inertia, $J_{3C(0)}$, become negligible. Further neglecting the distributed couple $\hat{m}_3$ in Eq. (A.5), the shear force $N_2(S,t)$ is expressed by the S-derivative of moment:

$$N_2(S,t) = \frac{\partial}{\partial S} M_3(S,t). \tag{A.7}$$

Rewriting Eq. (A.4b) using Eq. (A.9), the equation of motion for $u_2(S,t)$ becomes

$$\frac{\partial^2}{\partial S^2} M_3(S,t) + \hat{n}_2(S,t) = \mathsf{m}_{\mathsf{A}(0)} \frac{\partial^2 u_2(S,t)}{\partial t^2}. \tag{A.10}$$

The constitutive relation for moment is obtained by substituting Eq. (A.7) into Eq. (A.8):

$$M_3(S,t) = E I_3 \frac{\partial^2}{\partial S^2} u_2(S,t). \tag{A.11}$$

The axial equation of motion for $u_1(S,t)$ remains the same as that for the Timoshenko beam: Eq. (A.4a) and Eq. (A.6a), which are decoupled from the transverse deformation of the beam.

The analytical solutions are available for the Euler-Bernoulli beams to validate nonlinear FE beam codes and comparing the solutions with those of the Timoshenko

beams, one can assess the validity of neglecting the effect of transverse shear deformation.

Chapter 2, in part, has been submitted for publication of the material as it may appear in the International Mechanical Engineering Congress and Exposition 2017. Rios, Oscar; Amini, Ardavan; Murakami, Hidenori.

CHAPTER 3: AQUATIC ROBOT

3.1 Initial Prototype

3.1.1 Design

The robot, unlike other previously proposed methods, uses gyroscopes as a means of propulsion. By securing a gyroscope within the robot and operating the rotor at relatively high angular velocities, the rocking of the gimbal creates a gyroscopic moment on the body. By oscillating the gimbal while the rotor is spinning, the body can be made to oscillate, moving the caudal-like fin attached to the end of the body. These oscillations can be controlled to achieve maneuverability along the water surface plane.

As shown in Fig. 3.1 below, assuming the rotor is spinning counter clockwise (red arrow demonstrating the angular velocity vector), exciting the gimbal either with an angular velocity vector (green arrow) to the left or to the right will result in the body rotating to the left and right respectively.

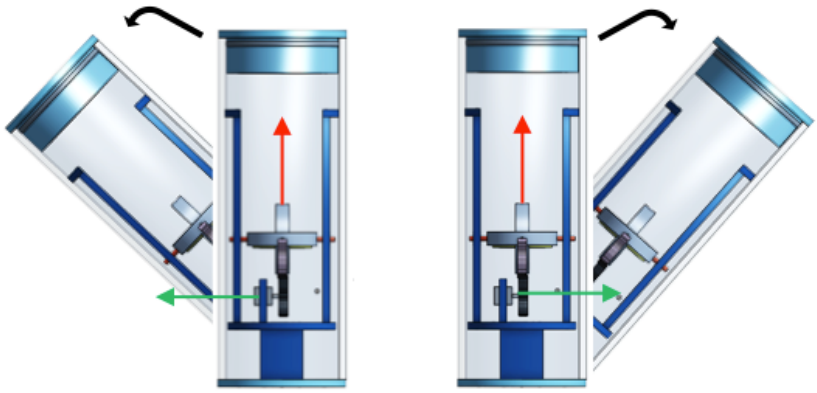

Figure 3.1: Model of the gyroscopically driven robot showing the basic principles used in turning and driving the robot

The robot has three major parameters that can be used to optimize both the speed and accuracy of its movements: the RPM of the rotor, the frequency of excitation, and the amplitude of the excitation. By controlling the three inputs, the robot can achieve precise turns and control the speed at which it moves in the forward direction.

The interior of the initial prototype as shown in Fig. 3.2 consists of an acrylic frame, an off-the-shelf gyroscope with an attached motor to operate the rotor, a servo to excite the gyroscope, a microcontroller along with an XBee module for wireless communication, and lithium-polymer batteries.

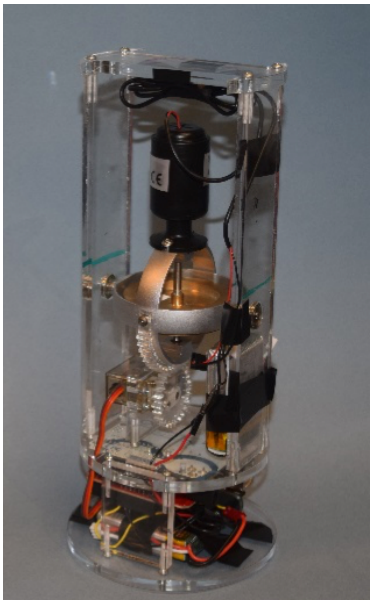

Figure 3.2: Interior of the robot containing an acrylic frame with a gyroscope and motor for the rotor, servo, microcontroller, XBee module, and Li-ion batteries.

The exterior of the body consists of a hard but lightweight cylindrical casing as shown in Fig. 3.3. To waterproof the cylinder, two end caps are used at either end. On one of the end caps is a 3D printed clamp that allows the fin to be easily interchanged for testing. As shown in Fig. 3.3, the blue strip placed down the middle allows for the correct orientation of the interior components. Since we are using the gyroscopic moment created around the third axis perpendicular to the two excited axes, it is important to properly align the gyroscope as shown in the model in Fig. 3.1. To further aid in keeping the robot stabilized and the gyroscope correctly aligned, small outriggers were 3D printed and attached to the cylinder. The fully assembled robot weighs 3.4 lbs. and is approximately a foot in length with a casing outer diameter of four inches.

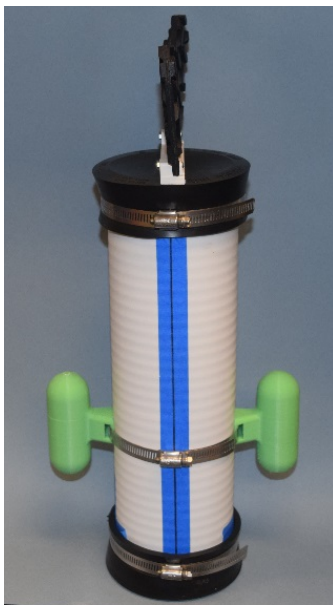

Figure 3.3: Fully assembled initial prototype

3.1.2 Experimental Results

Experiments were conducted to test the capabilities of the gyroscopically driven robot. The goals of the experiments were to see if we could accurately maneuver the robot anywhere along the water surface plane of the pool. The first task was to examine if the robot could accurately rotate 90 degrees in both directions so it could be maneuvered once moving in the forward direction. The first test conducted, as can be seen by the three snapshots of the video in Fig. 3.4, was a 90 degree right turn. The right turn was achieved by moving the gyroscope as shown on the right picture in Fig. 3.1. Holding the angular velocity of the rotor constant, the full 90 degree turn can be achieved in a time ranging from four to six seconds, depending on the rate at which the gimbal is moved. Moving the servo with and without a delay surprisingly led to a very small difference in the rate at which the robot reached the 90 degrees. When the gimbal was excited at a faster rate, the

robot experienced a higher initial acceleration, but the higher fluid resistance led to a faster deceleration once the gyroscope reached the maximum angle allotted. Exciting the gyroscope slowly not only provided a smooth 90 degree turn, but also allowed for very accurate turning when smaller angles were needed.

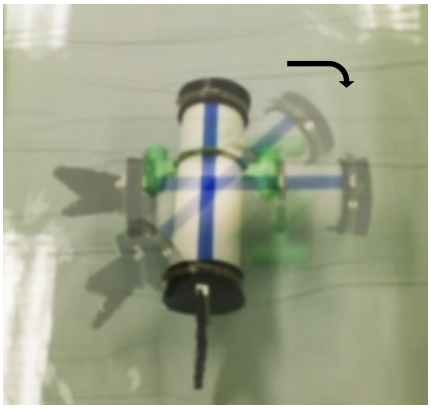

Figure 3.4: Three snapshots of the video file showing the 90 degree right turn

The left 90 degree turn was also completed successfully as shown in Fig. 3.5 below. To achieve the left turn, the gimbal was moved as shown on the left picture in Fig. 3.1. As with the right turn, the left 90 degree turn was performed at the same rate.

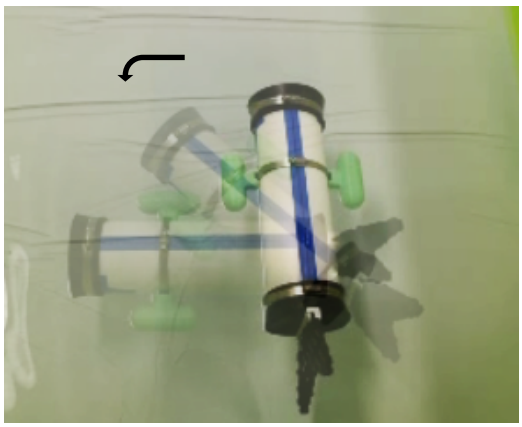

Figure 3.5: Three snapshots of the video file showing the 90 degree left turn

The next tests conducted were for a complete right and left 180 degree turn with a single excitation. If the angular velocity of the rotor is kept at very high speeds, the robot becomes very sensitive to any gimbal excitation. This not only aids in achieving very precise rotations, but it can also aid in completing higher degree turns. By exciting the gimbal slowly, full 180 degree turns were achieved in both direction as can be seen below in Figs. 3.6a and 3.6b. Both turns took on average 15 seconds to complete. Unlike with the smaller turns performed, the robot occasionaly slightly drifted from its initial starting position.

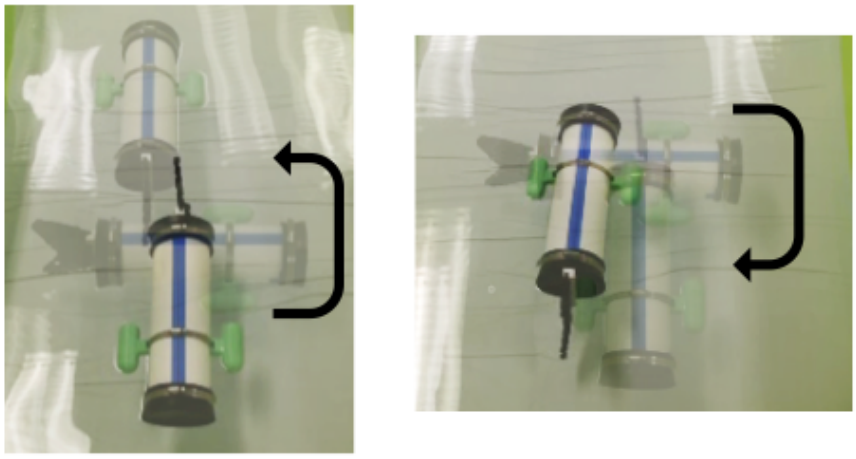

(a) (b)

Figure 3.6: Snapshots (a) Showing a left 180 degree turn and (b) 180 degree turn to the right allowing the robot to reverse in direction

The third test conducted was for the forward capabilities of the robot. To move along a straight path, the gimbal was rocked sinusoidally. The frequency of the oscillations was very important in achieving forward motion along a straight path. The nominal period for the tests of this initial prototype was approximately two seconds. Shown in Fig. 3.7 are

the snapshots of the robot as it traveled along the pool. On average, the robot completed the straight path test run at a rate of 1.5 in/sec.

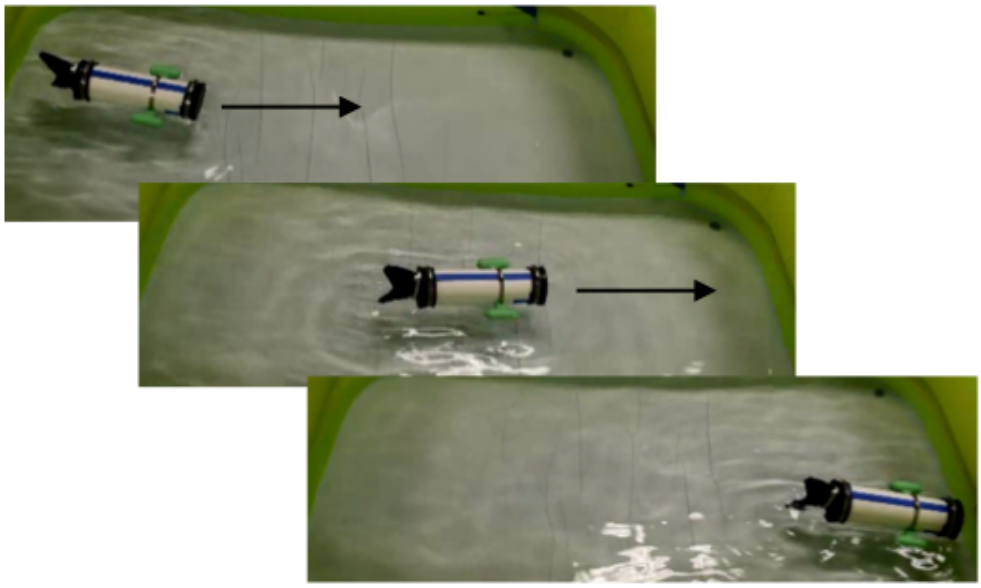

Figure 3.7: Snapshots of the test demonstrating the gyroscopically driven robot moving forward in a straight path

As the last test conducted, the robot was made to swim a lap around the pool, combining both the 90 degree right turns and the forward motion. It was able to finish the lap around the pool measuring 6ft×3ft in approximately 2 minutes and 30 seconds.

The robot can be greatly improved from the initial design, but it showed great promise, as it was able to maneuver along a 2D plane. The body, especially the end caps, can be more hydrodynamically designed to aid when swimming along a straight path. The initial design was wirelessly controlled but work is being conducted on making it autonomous.

3.2 Aquatic Robot With Caudal Fin

To increase the efficiency of propulsion from the initial design, an acrylic ribbed caudal fin is attached to the body.

3.2.1 Design

Since the initial test proved accuracy in rotation but inefficiency for forward motion, the final design focuses on optimizing the propulsive force of the aquatic robot. Using the acrylic fin used for the initial, in-air, caudal fin experiments, a final prototype was developed. The body and fin were connected using a 3D printed ABS rig. This allowed for rotation at the edge of the fin (similar to the initial experiments of the ribbed caudal fin). In Fig. 3.8, the final prototype can be seen.

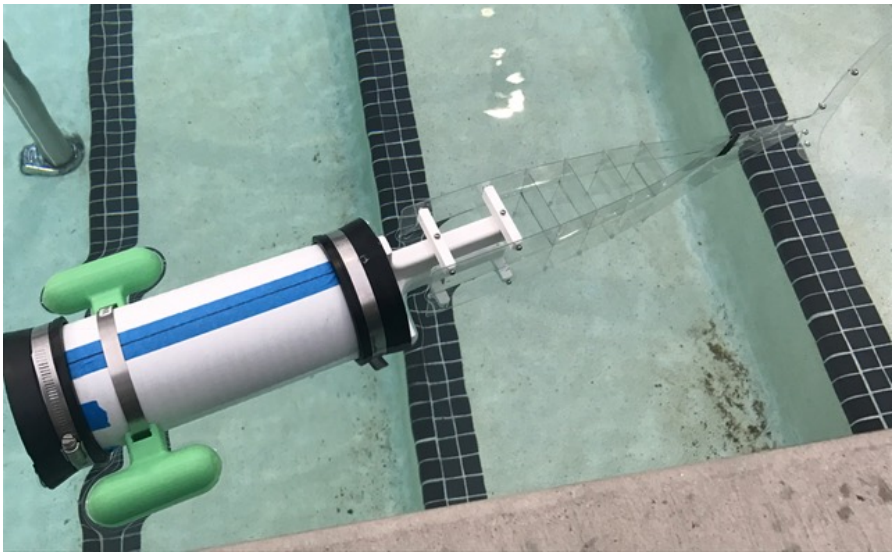

Figure 3.8: Final fish prototype including ribbed caudal fin

Because of this longer overall design, the robot had to be tested in a larger body of water rather than the original water tank.

3.2.2 Experimental Results

Experiments were conducted to test the efficiency of the aquatic robot including the ribbed caudal fin. The main focus was to achieve a faster speed than the initial tests, which yielded an average of 1.5 in/s, and having a more natural fish-like motion. Two tests were conducted, and the first test can be seen in Fig. 3.9.

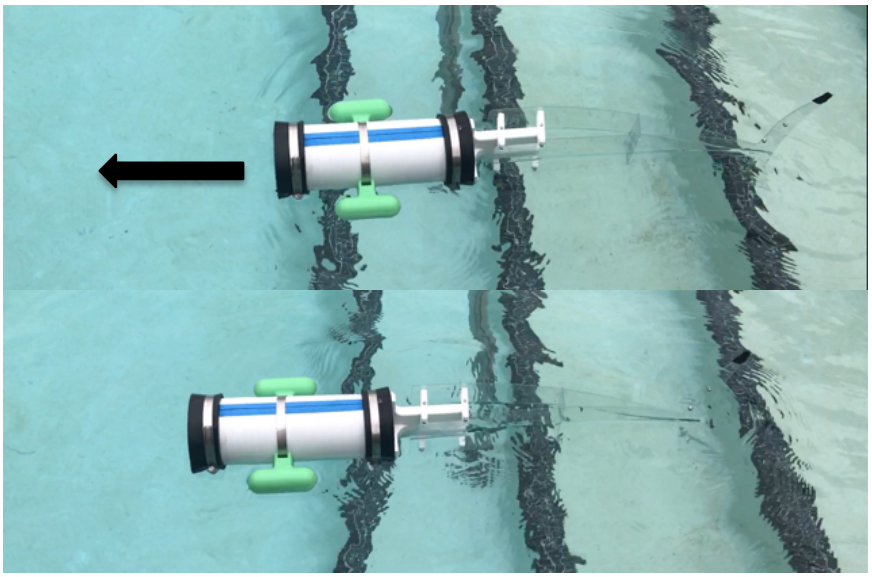

Figure 3.9: Snapshots of final prototype with a single rib moving forward in a straight path

The single-rib configuration achieved an average speed of 1.7 in/s. With this result, there were a few issues: The experiment was not as controlled as the initial water tank tests, there was mid-fin deflection that was not apparent in the in-air experiments for the caudal fin, and drag played a huge factor. In the initial water tank tests, the only waves reflecting back were due to the fish body's propulsive force, but the final prototype tests

had small waves propagate from multiple sources. In addition, the mid-fin deflection pointed to a lack of rigidity in the caudal fin, which was not an issue in the caudal fin experiments. Drag was also caused because the fin was not enclosed, so water filled the mid-section and prevented more propulsive force from being exerted. Also due to the drag, the accuracy of rotation was lessened. Although these issues prevented a much faster speed, the consistency of movement was adequate (i.e. it did not drift from its straight path).

To lessen the mid-fin deflection, a second test was conducted using a multi-rib configuration. In Fig. 3.10, the multi-rib test can be seen as it progressed through the water at a rate of 1.9 in/s.

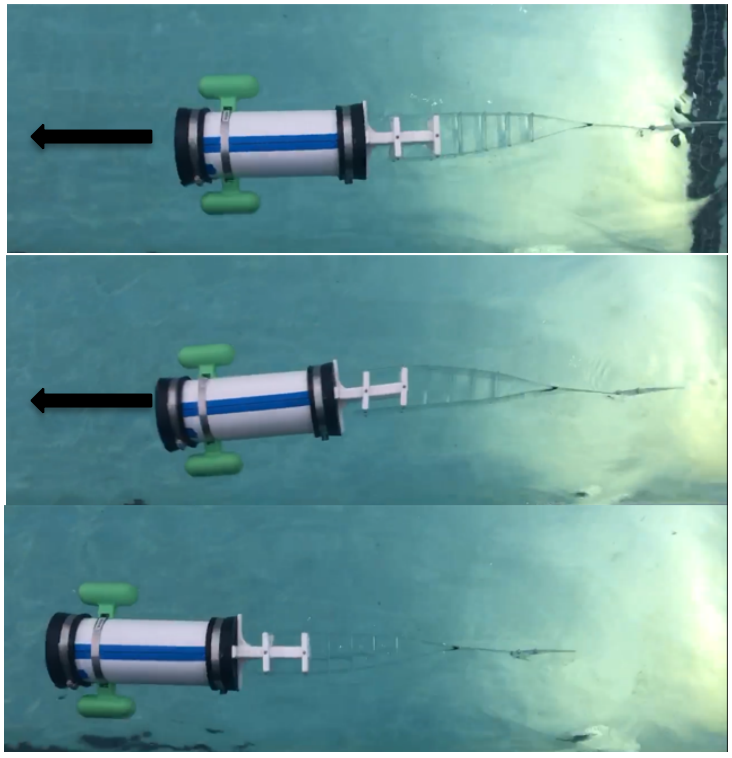

Figure 3.10: Snapshots of final prototype with multiple ribs moving forward in a straight path

The slight increase in speed shows that the deflection from the single-rib test did affect the propulsive force of the fin itself, which was not an apparent issue in the in-air fin tests, which led to conclusions that the locations of the ribs were more of a factor than the number of ribs. This realization pointed to a lack of focus on fluid-structure interaction in the initial caudal fin modeling and experiments.

Another revelation from these experiments was that the design could have been improved by changing the fin's point of actuation. The final prototype had the rotation point of the fin at the end of the gyroscopically driven robot body. However, the gyroscope generating the moment to propel the body back and forth rotated around the center of the body, so having the fin rotate closer to the center of the body may have yielded better results closer to that of the in-air fin experiments. Then, the deflections could have matched better. In any case, the addition of the caudal fin increased the speed by a maximum of 26.7%.

CONCLUSION

In chapter 2, it was shown that curved-beam models could be developed for a ribbed caudal fin, which was defined as two thin beams. The models were then compared to real-world experiments that actuated an acrylic ribbed caudal fin with multiple rib configurations at specified frequencies. Both the models and the experiments were done in-air assuming they would translate to water tank tests appropriately. However, that assumption was challenged in chapter 3.

Chapter 3 featured the design and experimentation of a gyroscopically driven aquatic robot without, and with, the ribbed caudal fin. The initial tests with a semi-rigid rubber fin achieved an average speed that could have been improved, so the ribbed caudal fin was implemented. Even though the speed only increased by 26.7% with the ribbed caudal fin, the experiments gave a lot of insights into how to optimize the system and hopefully create a system that could be used for surveillance and data collection as it was intended.

Some takeaways from the experiments included having to account for the fluid-structure interactions for more realistic results, as the in-air experimental deflection did not match up with the in-water experiments. Additionally, the accurate rotations of the robot were achieved with the initial design that did not have much drag, but the final prototype had issues, again, due to drag.

For future iterations of the aquatic robot, it will be important to incorporate the following design and experimental features: Having the rotation point of the fin closer to the gyroscope, which is where the moment is generated; using multiple ribs for the caudal

fin and/or enclosing said fin to reduce the drag within; testing the fish in a controlled environment without outside waves interfering in the data collection process; optimizing the stiffness/thickness of the material through the modeling to see what is most efficient.

This work has shown that there is a future for aquatic robots not just driven the conventional ways using multiple servos, hydraulics, and so on. Also, the combination of mathematical modeling and experimentation will be vital to the field's success with respect to validation and optimization.

REFERENCES

[1] Liu, J., Dukes, I. and Hu, H., 2005, August. "Novel mechatronics design for a robotic fish". In *Intelligent Robots and Systems, 2005.(IROS 2005). 2005 IEEE/RSJ International Conference on* (pp. 807-812). IEEE.

[2] Liu, J., Dukes, I., Knight, R. and Hu, H., 2004. "Development of fish-like swimming behaviours for an autonomous robotic fish". *Proceedings of the Control*, *4*, p.49.

[3] Arale, S., Pawar, C., Deshmukh, A., Dalvi, S., Pinjari, P. and Ohol, S.S., 2016, January. "Design and manufacture of Bio-mimic robotic fish". In *2016 IEEE First International Conference on Control, Measurement and Instrumentation (CMI)* (pp. 445-448). IEEE.

[4] Katzschmann, R.K., Marchese, A.D. and Rus, D., 2016. "Hydraulic autonomous soft robotic fish for 3D swimming". In *Experimental Robotics* (pp. 405-420). Springer International Publishing.

[5] Zhang, J., Tang, J., Hong, J., Lu, T. and Wang, H., 2014. "The Design and Analysis of Pneumatic Rubber Actuator of Soft Robotic Fish". In *Intelligent Robotics and Applications* (pp. 320-327). Springer International Publishing.

[6] Love, A. E., 1934, *A Treatise on the Mathematical Theory of Elasticity*, 4th edition, Chapter XIX, Cambridge.

[7] Reissner, E., 1972, "On One-Dimensional Finite-Strain Beam Theory: the Plane Problem," *Journal of Applied Mathematics and Physics (ZAMP)*, Vol. 23, pp. 795-804.

[8] Rios, O., Ono, T., and Murakami, H., 2016, "Development of Active Mechanical Models for Flexible Robots to Duplicate the Motion of Inch Worms and Snakes," *Proceedings of the 2016 IMCEC Conference*, Paper IMECEE2106-65550.

[9] Murakami, H., 2017, "Development of an Active Curved Beam Model—Part II: Kinetics and Internal Activation," *ASME Journal of Applied Mechanics*, Vol. 84, No. 6, 061003; also Murakami, H., 2016, "Development of an Active Curved Beam Model Using a Moving Frame Method," *Proceedings of the ASME 2016 International Mechanical Engineering Congress & Exposition*, paper IMECE2016-65294, 17 pages.

[10] Hughes, T. J. R., 1987, *The Finite Element Method, Linear Static and Dynamics Finite Element Analysis*, Prentice Hall, Englewood Cliffs. NJ.

[11] Belytschko, T., Liu, W. K., and Moran, B., 2000, Nonlinear Finite Elements for Continua and Structures, John Wiley & Sons, New York.

[12] Kirchhoff, G., 1859, “Über das Gleichgewicht Unad die Bewegung eines Unendlich Dünnen Elastischen Stabes, *J. Reine u. Angrew. Math*., 56, pp. 285-313.

[13] Frankel, T., 2012, *The Geometry of Physics, an Introduction*, 3rd edition, Cambridge, New York.

[14] Fung, Y. C., 1965, *Foundation of Solid Mechanics*, Prentice-Hall, Englewood Cliffs, NJ.

[15] Reissner, E., 1945, “The Effect of Transverse Shear Deformation on the Bending of Elastic Plates,” *Journal of Applied Mechanics*, Vol. 12, pp. A69-A77.

[16] Reddy, J. N., 1993, *An Introduction to the Finite Element Method*, 2nd edition, McGraw-Hill, New York.

[17] Rios, O., Murakami, H., 2015, "A mathematical model of an active gyroscopic roll stabilizer using the moving frame method," *Proceedings of the ASME 2015 International Mechanical Engineering Congress & Exposition*, paper IMECE2015-51157.

[18] Murakami, H., Rios, O., 2013, "A mathematical model for a gyroscopic ocean wave energy converter," *Proceedings of the ASME 2013 International Mechanical Engineering Congress & Exposition*, paper IMECE2013-62834.

[19] Murakami, H., Rios, O., Amini, A., 2015, "A mathematical model with preliminary experiments of a gyroscopic ocean wave energy converter," *Proceedings of the ASME 2015 International Mechanical Engineering Congress & Exposition*, paper IMECE2015-51163.

[20] Townsend, N., Murphy, A., and Shenoi, R., "A new active gyro stabilizer system for ride control of marine vehicles," *Ocean Engineering*, vol. 34 no. 11-12, pp. 1607-1617, 2007.